NTNU

Norwegian University of
Science and Technology

Comparison Between Microstructure Parameters and Electrochemical Performance of Ni-CGO Anodes in SOFC Subjected to Redox-Cycling

Jørgen Svendby

Chemical Engineering and Biotechnology
Submission date: August 2011
Supervisor: Svein Sunde, IMTE

Norwegian University of Science and Technology
Department of Materials Science and Engineering

NTNU – Trondheim
Norwegian University of
Science and Technology

MASTER'S THESIS
IN
ELECTROLYSIS AND MATERIALS SCIENCE

Comparison Between Microstructure Parameters and Electrochemical Performance of Ni-CGO Anodes in SOFC Subjected to Redox-Cycling

by

JØRGEN SVENDBY

Supervisors:

PROF. SVEIN SUNDE, NTNU
PROF. THOMAS GRAULE, EMPA
PROF. THOMAS HOCKER, ZHAW
DR. LORENZ HOLZER, EMPA
DR. BORIS IWANSCHITZ, HEXIS AG

NTNU
Faculty of Natural Sciences and Technology
Department of Materials Science and Engineering

EMPA
Swiss Federal Laboratories for Materials Science and Technology
High Performance Ceramics

Dübendorf, August 8, 2011

Preface

This master thesis is submitted as the final fulfillment of the requirements for the Master of Science in Technology (MSc) degree at the Norwegian University of Science and Technology (NTNU). The work has been carried out at the Swiss Federal Laboratories for Materials Science and Technology (EMPA) at the High Performance Ceramics department under the main supervision of Dr. Lorenz Holzer. The work was performed in close cooperation with Hexis AG. and Zurich University of Applied Sciences (ZHAW). The work was conducted between 1. of February to the 31. of July at EMPA Dübendorf.

I will thank all my supervisors for the valuable guidance and help that I have received during this work. A special thank to Dr. Lorenz Holzer for being available most of the time when I needed guidance.

Abstract

The aim of this thesis was to create an understanding between the electrochemical performance of a porous Ni-CGO anode used in SOFC, and its microstructural parameters when subjected to redox-cycling. The anode samples were produced consisting of two different layers, and subjected to different number of redox-cycling. Their electrical resistance was measured using electrochemical impedance spectroscopy (EIS), and their parameters were obtained by analyzing cross-section images from the samples obtained by the focused ion beam (FIB) or from simulated 3D-models. A large increase of ohmic resistance was observed after 3-4 redox-cycles, while there was only a slight increase of the polarization resistance. The high increase of the ohmic resistance is believed to be due to the observed Ni-coarsening and the net increase of the anode volume due to oxidation of Ni to NiO and subsequently reduced back to Ni. Both the Ni-coarsening and the net volume expansion decrease the Ni connectivity which increases the ohmic resistance. More electrons are also forced to go through the lower-conducting CGO phase, which increases the ohmic resistance, though preventing a higher increase since it is connecting the isolated Ni grains together. The low increase of polarization resistance is believed to be due to the large pore-CGO interfacial area, which compensates for the decrease in triple-phase boundaries (TPB). The resolution of synthetic microstructures is not enough to capture constrictivity and tortuosity effects realistically. The dimensions of most of the bottle necks are below 100 nm and hence the size classes must be in the range of 10 nm, which is similar as the resolution of FIB-tomography.

Contents

List of Symbols **6**

Abbreviations **8**

1 Introduction **9**

2 Theory **12**
2.1 Microstructural Principles and Analysis Techniques 12
2.1.1 Microstructural Parameters 12
2.1.2 Image Segmentation 15
2.1.3 Continuous Phase Size Distribution (PSD_c) 16
2.2 Microstructural Analysis Tools 18
2.2.1 Carbon Thread Coating 18
2.2.2 Scanning Electron Microscope (SEM) 19
2.2.3 Focused Ion Beam (FIB) 20
2.3 Electrochemical Principles and Techniques 21
2.3.1 Ohmic- and Polarization Resistance 21
2.3.2 Area-Specific Resistance (ASR) 22
2.3.3 Electrochemical Impedance Spectroscopy (EIS) 23
2.4 Microstructure Modeling of SOFC Anodes: Synthetic Microstructues for FEM 25

3 Experimental **26**
3.1 Sample Preparation 26
3.1.1 Anode Fabrication and RedOx-Cycling 26
3.1.2 Sample Processing 27
3.1.3 Carbon Coating Process 28
3.2 Sample Imaging 29
3.2.1 Scanning Electron Microscope (SEM) 29
3.2.2 Focused Ion Beam (FIB) 29
3.3 Sample Analysis 30
3.3.1 Image Segmentation 30
3.3.2 Microstructural Parameter Extractions 31
3.3.3 Electrochemical Impedance Spectroscopy (EIS) 32

4 Results **33**
4.1 Qualitative Comparison Between FIB Cross-Sectional Images 33
4.2 Continuous Phase Size Distributions (PSD_c) 34
4.3 Volume Fractions 38
4.4 Phase Surface Area 39
4.5 Phase Interfacial Area 40

4.6 Triple Phase Boundary (TPB) Changes 41
4.7 Electrochemical Impedance Spectroscopy Results 43
4.8 Analysis of Synthetic 3D-Microstructures 44

5 Discussion **47**

6 Conclusions **49**

7 References **50**

Appendices **54**

A Comparison of SEM- and FIB-Results **54**

B Connectivity Calculations **57**

List of Symbols

Symbol	Unit	Description
A	cm^2	Cross-sectional area of the conductor
$A_{fuelcell}$	cm^2	Fuel cell area
A_{max}	cm^2	Non-constricted cross-sectional area of conductor
A_{min}	cm^2	Constricted cross-sectional area of conductor
ASR	$\Omega \cdot \mathrm{cm}^2$	Area-Specific Resistance
D_b	$\frac{cm^2}{s}$	Normal diffusion coefficient
D_e	$\frac{cm^2}{s}$	Effective diffusion coefficient
F	$\frac{C}{mole}$	Faraday's constant
i	A	Current
i_0	A	Amplitude of the current
j	$\frac{A}{cm^2}$	Current density
j_0	$\frac{A}{cm^2}$	Exchange current density
j_{im}	-	Imaginary number
l	cm	Linear length of charge transport
l_e	cm	Real length of charge transport
n	-	Electron transfer coefficient
R	$\frac{J}{K \cdot mole}$	Gas constant
R_b	Ω	Normal ohmic resistance
R_e	Ω	Effective ohmic resistance
R_{elec}	Ω	Electrical resistance
R_{ionic}	Ω	Ionic resistance
R_{ohmic}	Ω	Ohmic resistance
R_p	Ω	Polarization resistance
R_{tot}	Ω	Total resistance
r_{max}	cm	Non-constricted radii of conductor
r_{min}	cm	Constricted radii of conductor

Symbol	Unit	Description
T	K	Absolute temperature
t	s	Time
V	V	Voltage
V_0	V	Amplitude of the voltage
Z	Ω	Impedance
Z_0	Ω	Fraction of V_0 and i_0
Z_{fA}	Ω	Anodic activation losses from EIS data
Z_{fc}	Ω	Cathodic activation losses from EIS data
Z_Ω	Ω	Ohmic losses from EIS data
α	-	Transfer coefficient
δ	-	Constrictivity
ϵ	-	Porosity
η_{act}	V	Activation voltage loss
η_{ohmic}	V	Ohmic voltage loss
σ	S	Conductivity
σ_b	S	Normal conductivity
σ_e	S	Effective conductivity
τ	-	Tortuosity
Φ	-	Volume fraction
ϕ	-	Phase shift between V and i
ω	s^{-1}	Angular frequency

Abbreviations

Abbreviation	Description
BSE	Back-Scattered Electrons
CGO	Ceria Gadolinia Oxide
EIS	Electrochemical Impedance Spectroscopy
ESB	Energy and angle Selective Backscattered electron detector
ETD	Everhart-Thornley Detector
FEM	Finite Element Modeling
FIB	Focused Ion Beam
GIS	Gas Injection System
HV	High Voltage
LMIS	Liquid Metal Ion Source
MIP	Mercury Intrusion Porosimetry
PSD	Phase Size Distribution
PSD_c	Continuous Phase Size Distribution
SE	Secondary Electrons
SEM	Scanning Electron Microscope
SOFC	Solid Oxide Fuel Cell
TPB	Triple-Phase Boundary
vCD	low voltage high Contrast Detector
WD	Working Distance
YSZ	Yttrium-Stabilized Zirconia

1 Introduction

A fuel cell is a device that transforms chemical energy directly to electrical energy[1]. A fuel cell can in a simplified way be seen as a device that produces electricity without being consumed itself in contrast to batteries[1]. As long as sufficient fuel (reactants) is added, the fuel cell will deliver a constant flow of electricity (this is only in an ideal situation).

The principle of the fuel cell was first demonstrated by Sir William Grove in 1839[2][3]. Since then a lot of improvements and a successfully deployment in the American Apollo space program have followed, but the commercial breakthrough has yet to be achieved[3]. But in the recent years the interest for fuel cell technology has been increasing. The reason for this is that fuel cells have some advances over batteries and combustion engines (which are the main options to fuel cells) or share the advantages from both of them[4]. Among these are the high fuel efficiency, lower emissions of harmful gases (CO_2, NO_x, and SO_x), does not have to be recharged, and have a potential to be a long lasting and stable system for electricity deliverance[4]. There are also different types of fuel cells, each with distinct advantages and disadvantages.

The present study is dealing with the solid oxide fuel cell (SOFC), which has a solid ceramic electrolyte and it operates at high temperatures[5]. The electrolyte is made of a ceramic where yttria-stabilized zirconia (YSZ) is by far the most used material. Above a temperature of about 800 ^oC, YSZ starts to be a conductor for the charge carrier (O^{2-}) and the operating temperature therefore needs to be relatively high, usually between 800 to 1100 ^oC[6]. The high operating temperature gives the SOFC some advantages and disadvantages. The high temperature ensures relatively fast reaction kinetics, which makes it unnecessary to use precious metal electrocatalysts[6][7]. A wide variety of fuels can be used including carbon monoxide (CO) which acts as a poison in low temperature fuel cells[5][6]. The SOFC has a high electrical efficiency (50-60 %) and by exploiting the excess heat, the efficiency can potentially reach 90 %[5]. The fact that no liquid is present in the cell ensures that corrosion problems and other complications handling liquids are not present[6][7]. Material requirements, mechanical issues, and the matching between the thermal expansion of the different materials are some of the problems[5]. Also since most of the cell parts are made of ceramics in order to be stable at high temperatures, the price increases because of the expensive fabrication and materials costs[5].

One of these parts is the anode that has as its primary role to promote the electrochemical oxidation of fuels[8]. The anode is one part of the cell which is affected by the high temperature operation. Since the anode has to conduct electrons, it has to consist of an electron conductor (normally a metal). The metal has normally been Nickel (Ni) because of its good chemical stability, high catalytic activity toward hydrogen oxidation, good reforming of hydrocarbon fuels, and its relatively low price[8]. But the problems

using Ni are the thermal expansion mismatch between Ni and other cell parts, and that Ni coarsens during the high temperature operation[8]. These degradation processes destroy the original anode structure, which leads to a reduction of the efficiency or even to complete failure of the cell. The conventional SOFC anode consists of a porous mixture between a metal and a ceramic (a so-called cermet), where the ceramic is normally YSZ or ceria gadolinia oxide (CGO)[5][6][8][9]. The main role of the ceramic is to stabilize the metal and preventing it from coarsening[8]. Other roles are conducting ions to the metal, and reducing the thermal expansion mismatch between the anode and other cell components[8]. The porosity ensures that the different reactant and product gases can enter and leave the anode respectively[8].

Exceeding 40 000 operation hours is needed to successfully commercialize SOFC. So far this has not yet been achieved[9]. This is due to changes in the microstructure of the SOFC during operation whereby anode degradation represents a major problem[9][10]. Among the degradation mechanisms for Ni-cermet anodes are coking (carbon deposition on the anode surface), sulfur poisoning, and redox-cycling[9][10][11]. Grain growth of Ni normally affects the cell performance due to the reduction of the triple-phase boundaries (TPB) in the anodes[10]. The TPBs are reaction sites where the three different phases of the anode meet and where it is believed that most of the electrochemical reactions takes place (the electrons, ions, and the reactant gases all have access to the active TPBs)[8].

To be able to increase the operation hours of the SOFC, an understanding of the relationship between the anode performance (electrochemical performance, sections 2.3.1 and 2.3.2) and the anode microstructure (section 2.1.1) needs to be established. The anode performance is governed by the effective transport by the three phases (diffusivity for the gases and conductivity for the ions and the electrons) and the reaction kinetics on the anode surface and the TPBs. Three important aspects which governs the transport are the tortuosity (the travel length of the gases, electrons, and ions), the constrictivity (reduction in the cross-sectional area of the different conductors), and the connectivity of the conducting phases which all are dependent on the microstructure[12]–[17]. Many properties influence the reaction kinetics, but material choice and active anode area (which in this context is normally synonymous with TPBs) are among the most important ones[18].

The aim of this work is therefore to try to understand the influence of the anode microstructure on the anode electrochemical performance, and in addition, also to improve our understanding of the degradation mechanisms associated with redox-cycling. In this work the microstructure and the electrochemical performance of Ni-CGO cermet anodes are investigated. Thereby the effect of redox-cycling on microstructure changes and associated performance losses are described quantitatively. The Ni-CGO cermet anode is among the most interesting SOFC-anodes, especially because CGO is a so-called mixed conductor (it conducts both electrons and ions, though the electron conductivity

is not as good as with Ni)[9]. The anodes consist of two layers, the active anode layer (which is facing the electrolyte in the fuel cell, and therefore has a finer structure to ensure efficient ionic conductivity and electrochemical activity) and the current collector layer (which is facing the incoming reactant gas(es), and is therefore more porous to ensure efficient gas diffusion)[19]. Redox-cycles (the change of gas-compositions that appear when the cell is stopped and restarted) has shown to be very destructive for the cell performance due to the not fully reversible volume expansion/contraction of the anode because of Ni reduction and oxidation[9][20]. In this study, different anode samples (lamellas) are subjected to different number of redox-cycles. Electrochemical impedance spectroscopy (EIS) measurements (section 2.3.3) are then performed to measure the ohmic- and the polarization resistances (R_{ohmic} and R_p respectively, section 2.3.1). From the measured voltage (V) and current (i) the total area-specific resistance (ASR) is calculated (section 2.3.2). The aim is to investigate the charge transport (which the R_{ohmic} is dependent on), the kinetics (which the R_p is dependent on), and the change of the total resistance which is independent of active surface area changes (which is the ASR). 2D-microstructural analysis is conducted on segmented images (section 2.1.2) from back-scattered electrons (BSE) taken by either the scanning electron microscope (SEM) or the focused ion beam (FIB). The phase-size distributions (PSDs, the percentage amount of each phase with the respect to the phase size, section 2.1.1) and the volume fractions of the different phases will be measured using the continuous phase size distribution (PSD_c)-method (section 2.1.3). Phase surface areas, phase interfacial areas, and TPBs (section 2.1.1) will be measured from the cross-sectional pictures (section 3.3.2). An average value from 4 to 5 images is used to ensure the representativity of the measurements. 3D-modeling (section 2.4) of the microstructure is performed to be able to measure the tortuosity and the constrictivity (section 3.3.2), since it is not possible to obtain them from 2D analysis[19].

2 Theory

2.1 Microstructural Principles and Analysis Techniques

2.1.1 Microstructural Parameters

Microstructural parameters are values that describe statistically the morphology (shapes of the different phases) on a grain-scale. For Ni-CGO cermet anodes there are many important microstructural parameters, but the ones in focus in this work are the phase-size distribution (PSD), triple-phase boundaries (TPB), surface areas of the different phases, interface areas between the different phases, volume fractions (Φ), tortuosity (τ), and constrictivity (δ). Particle shapes can partially be interpreted from the interface area- and surface area data, while connectivity can partially be interpreted by the percolation threshold (a characteristic volume fraction where there is connectivity above, and reduced connectivity below)[15][16][17].

The phase size distribution (PSD) is the percentage amount of each phase with respect to the corresponding phase size intervals (size classes). It can be measured as an area (2D) or as a volume (3D)[21]. The PSD is important in most types of material science since it affects the material properties such as material strength, porosity, and conductivity. Accurate calculations of PSDs are hard to achieve, and different methods can be used[10][21]. In this work the continuous phase size distribution (PSD_c)-method was used (section 2.1.3), and the PSD was measured in 2D.

Triple-phase boundaries are points (2D) or lines (3D) where all three phases of the anode meet each other[8][22]. In the ideal case, electrons, ions, and the reactant gas(es) all have access to the TPBs. The TPB is therefore regarded as the most important part of the electrode surface where most (if not all) electrochemical reactions take place[8][22]. In this work the TPBs were measured in 2D and normalized (divided) with the picture area (number of TPB-points per μm^2).

The phase surface area and the phase interfacial area are the surface area of an phase and the contact area between two phases respectively. They are measured as a length in 2D or as an area in 3D. In anodes with a mixed conducting phase the surface area of this phase can become electrochemically active[23]. A surface area can also tell something about the phase-sizes and the morphology. In this work they were both measured in 2D and normalized (divided) with the picture area $\left(\frac{\mu m}{\mu m^2}\right)$.

The volume fraction (Φ) of the different phases is a measure of the relative volumes of the different phases. In 2D it is measured as an area and in 3D as a volume. The volume fraction gives the amount of the different phases in the anode, which is important to control for optimum properties, like the TPBs, and to ensure phase connectivity (to ensure that the phases are continuously connected and not isolated)[23][24]. In this

work the volume fraction of the phases was measured in 2D using the PSD_c-method (section 2.1.3).

Tortuosity is normally thought of as the deviation from linearity of the transport path of charge (electrons or ions), or the path of diffusion of a substance (though it has no universal definition)[13]. It is illustrated in Figure 1 and given by equation 1:

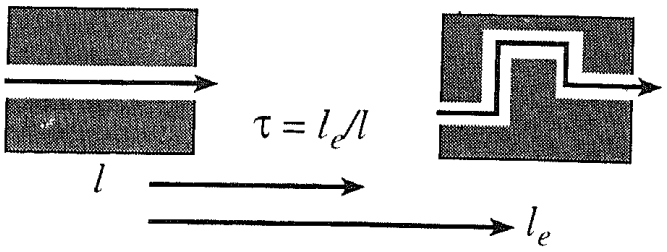

Figure 1: The principle of tortuosity with equation 1 (the Figure is obtained from [13]).

$$\tau = \frac{l_e}{l} \tag{1}$$

where l_e is the real length along the pore pathway and l is the linear length (equal to l in equation 7)[13]. If τ is 1 the transport path is linear. When it is larger the transport path is longer. The larger the value of τ the less linear (longer distance) is the transport path. A relationship between the ratio of diffusion coefficients (the effective diffusion coefficient and the normal diffusion coefficient), and the tortuosity has been established and is given by equation 2:

$$\frac{D_e}{D_b} = \frac{\epsilon}{\tau} \tag{2}$$

where ϵ is the porosity, D_b is the normal diffusion coefficient (the case for theoretically maximum transport media without microstructure effect when ϵ and τ equal 1), and D_e is the effective diffusion coefficient (the real diffusion coefficient when the ratio between ϵ and τ differ from 1) [12][25].

ϵ and τ explain often the deviations between D_e and D_b. But there has been observed that constrictions in the structure of the transporting phase may lead to an additional decrease of D_e. In literature the effect of constrictions is often included in the tortuosity (Figure 2) [13].

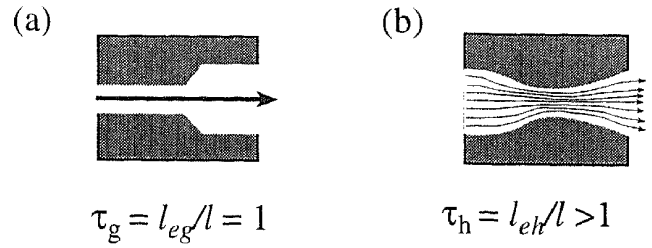

Figure 2: Principle of constrictivity. (a) shows a widening of the cross-section area where no reduction of the cross-section appears, (b) shows a reduction (constriction) of the cross-section area, and an increase in tortuosity (the Figure is obtained from [13]).

Hence, this constrictivity-effect is often an integrated part of the tortuosity constant, but some works have separated constrictivity from tortuosity as an own constant, with its definition given by equation 3:

$$\delta = \left(\frac{D_e}{D_b \epsilon} \right)_{\tau=1} \tag{3}$$

where δ is the constrictivity, and $\tau = 1$ [12][13][14]. Another version to equation 2 has been proposed given in equation 4:

$$\frac{D_e}{D_b} = \frac{\epsilon \delta}{\tau^2} \tag{4}$$

where the constrictivity is included[14]. In this work the constrictivity was measured in 3D from models (so-called synthetic microstructures) since measurements in 2D are not suitable for this purpose[19][23]. Thereby constrictivity is defined as the ratio of the constricted conductor cross-sectional area (A_{min}) over the non-constricted conductor cross-sectional area (A_{max}):

$$\delta = \frac{A_{min}}{A_{max}} = \frac{\pi r_{min}^2}{\pi r_{max}^2} \tag{5}$$

where r_{min} is the constricted radii of the conductor and r_{max} is the non-constricted radii of the conductor. Thereby r_{max} is obtained from the measurement of continuous PSD (r_{max} is defined as the radius corresponding to the so-called 50 % fraction of the cumulative PSD-curves). Furthermore r_{min} is obtained from the simulation of mercury intrusion porosimetry (MIP). Thereby r_{min} is defined as the radius corresponding to the 50 % fraction in the PSD obtained from the MIP. The PSD from the MIP is affected by the so-called ink-bottle effect which is caused by the phase necks. This is then used to quantify the constrictivity.

The degree of connectivity of the conducting phases can roughly be interpreted by the so-called percolation threshold[15][16][17]. The percolation threshold is a characteristic

volume fraction of the conducting phase, beyond which the connectivity is lost and consequently the conductivity is significantly reduced[15][16][17]. It is believed that when the volume fraction is below the percolation threshold value, there is not enough of the conducting phase to create connection between the electrolyte and the chemical active surface. Instead the phase is isolated in distinct particles. The volume fraction of the conductor phases is therefore always kept over the percolation point during production to ensure adequate conductivity.

2.1.2 Image Segmentation

Image segmentation is a method to divide different parts of a picture into different homogeneous pixel regions[26][27]. The result is a simpler picture whereby each phase is represented by a specific gray scale[26]. The simpler the original picture, the easier it is to perform image segmentation[26]. Problems arise when the original image is "noisy", low in contrast, affected by gray scale gradients (background), or other image defects. If the original picture is very complicated, an accurate segmentation of the image can be hard to achieve (much of the picture information may be lost). An illustration of image segmentation performed on a cross-section picture of a porous Ni-CGO anode can be seen in Figure 3.

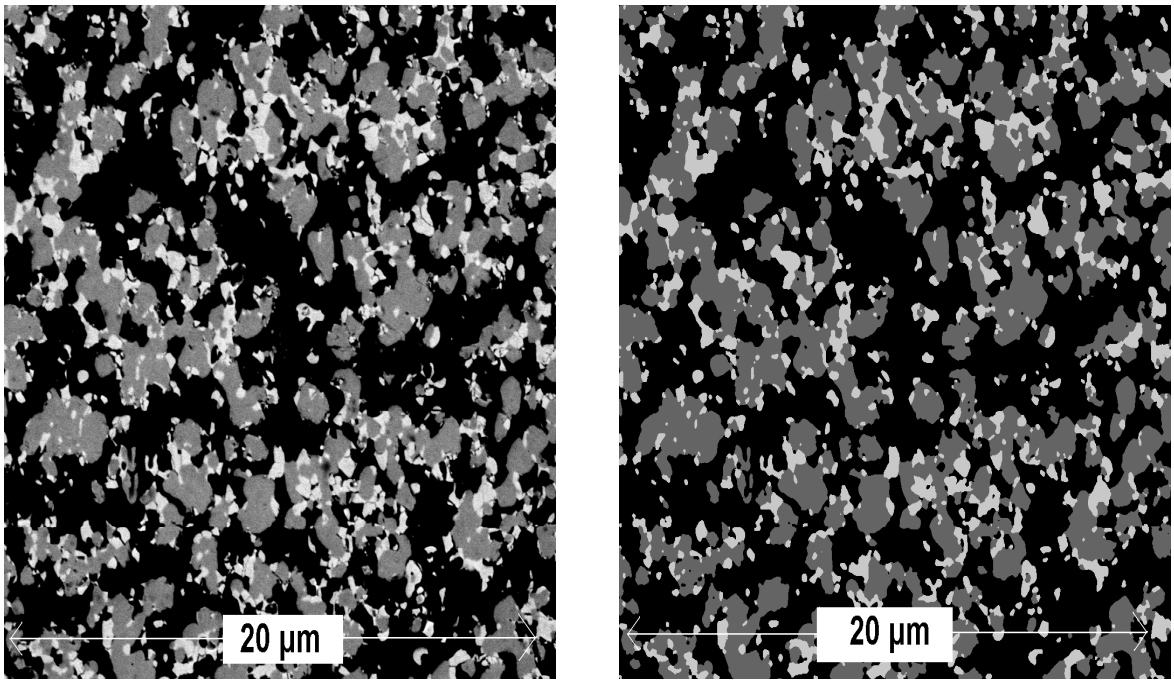

Figure 3: Left: Ni-CGO original BSE-picture obtained from the SEM. Right: the same picture which has undergone segmentation. The three phases, pores (black), Ni, (dark gray), and CGO (white gray) can be seen.

The picture to the left is the original BSE-picture taken by the SEM, the picture to the right is the end product from the image segmentation. As can be seen, "noise" in the picture to the left has been removed, and the different phases have a homogeneous colour and are separated from the other phases. As can also be seen, some phases from the original picture have wrongly been transformed to another phase in the segmented picture, but as long as not too much information is lost in segmentation, the final result will have an acceptable accuracy.

2.1.3 Continuous Phase Size Distribution (PSD_c)

Continuous phase size distribution (PSD_c) is one method to obtain phase size distribution (PSD) data from a sample[21]. This method became the outcome from an investigation of why the well established methods (mainly the mercury intrusion porosimetry (MIP) method and the investigation of BSE-pictures obtained by SEM) for deciding the pore size distribution deviated substantially[21]. The PSD_c-method can also be used to determine grain sizes and volume fractions, and it can be used for both 2D- and 3D-analysis[10]. Another advantage is that results from 2D are almost identical to results obtained from 3D[19]. The method is therefore easy to use since in 2D-analysis only cross-sectional pictures (usually BSE-pictures) of the sample surface are needed, instead of a volume needed for 3D-analysis, which is more complicated to obtain[19].

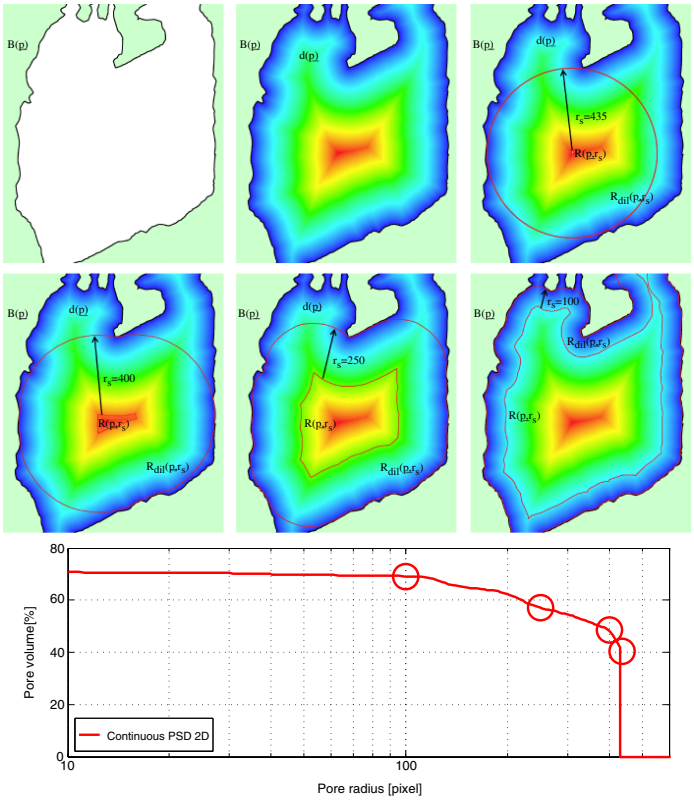

Figure 4: Illustration of the PSD_c-method in 2D. From the original picture (top left) the phase of interest is transformed into a distance map thereby the different pixels in the picture receive a colour based on their distance to the pore boundary (top center). A circle of maximum radius is fitted (top right) at the local maximum of the distance map. The radius is then reduced incrementally whereby more constricted areas can be formed by the smaller circle (bottom from left to right). The radius length is then plotted against the fraction of the total area of the picture which can be intruded at the given radius (figure obtained from [21]).

The principle of the PSD_c-method can be seen in Figure 4 where a single pore is depicted[21]. The algorithm for the PSD_c-measurement represents the simulation of mercury intrusion (with some modifications). The phase of interest is first transformed into a distance map. A circle (in 2D) or a sphere (in 3D) of maximum radius is then placed at the local maximum in the distance map (red). The radius is then reduced and the center of the sphere can be shifted within a certain area, whereby the perimeter of the area covered by the shifted sphere is still within the phase boundaries. By reducing the radius incrementally, the circle can be shifted over a larger area and it can intrude more constricted parts of the phase. At very small radii the entire phase can be covered by the shifting circle. A cumulative size distribution curve is then obtained by plotting the areas which are covered by the shifting circle at a given radius versus the corresponding

radii. In contrast to mercury intrusion the PSD_c is not affected by the so-called ink-bottle effect, since the intrusion process is not initiated at the sample boundaries. Instead the intrusion process is initiated at each local maximum in the distance map. An additional difference between mercury intrusion and PSD_c is that mercury intrusion only works for the pore size distribution, while PSD_c can also be used for solid phases.

2.2 Microstructural Analysis Tools

2.2.1 Carbon Thread Coating

For SEM or FIB investigations, non-conductive samples need to be coated by a charge-conducting material in order to avoid charge accumulation on the sample surface. Carbon thread coating is a method to increase the conductivity of samples by coating them with a carbon layer[28]. Previously, coating of samples has been done by evaporating carbon from sharpened carbon rods under vacuum conditions[28]. But because not all of the carbon becomes degassed, carbon pieces are sputtered on the sample which leads to artifacts[28]. Another problem is also that the films does not fully envelop the surface structures[28].

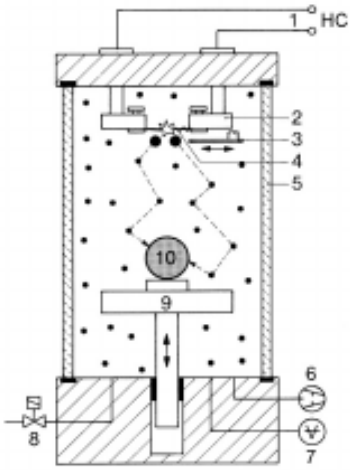

Figure 5: Principle of carbon thread coating. 1 is the high current supply, 2 is the quick mounting holder, 3 is a movable shutter, 4 is the carbon thread, 5 is the vacuum chamber barrier, 6 is the pump, 7 is the vacuum gauge head, 8 is the automatic venting device, 9 is the adjustable specimen table, and 10 is the sample. The small black dots are gas molecules from gases still present in the chamber, and the big black dots are carbon atoms released from the carbon thread (the Figure is obtained from [28]).

The principle of carbon thread coating is shown in Figure 5. Carbon threads are fastened to two different high current electrodes. Under vacuum conditions in the chamber, high current is passed through the carbon threads making them burn and

evaporate[28]. The carbon collides with the gas molecules still present in the chamber, spreading them out into a diffuse cloud of carbon atoms. The atoms are then condensing evenly on the sample surface, making a uniform, fine grained, and electrically conductive layer[28].

2.2.2 Scanning Electron Microscope (SEM)

The scanning electron microscope (SEM) is a microscope that uses a ray of electrons to gather information from the sample[29]. The principle of the SEM operation is shown in Figure 6 (left). The electrons are sent out in a focused beam from an electron gun and onto the sample. The beam is being swept over the sample surface from point to point in a rectangular raster pattern (Figure 6) [29]. Since the electrons would have been deflected and losing energy hitting other molecules, the operation needs to be performed in vacuum[29].

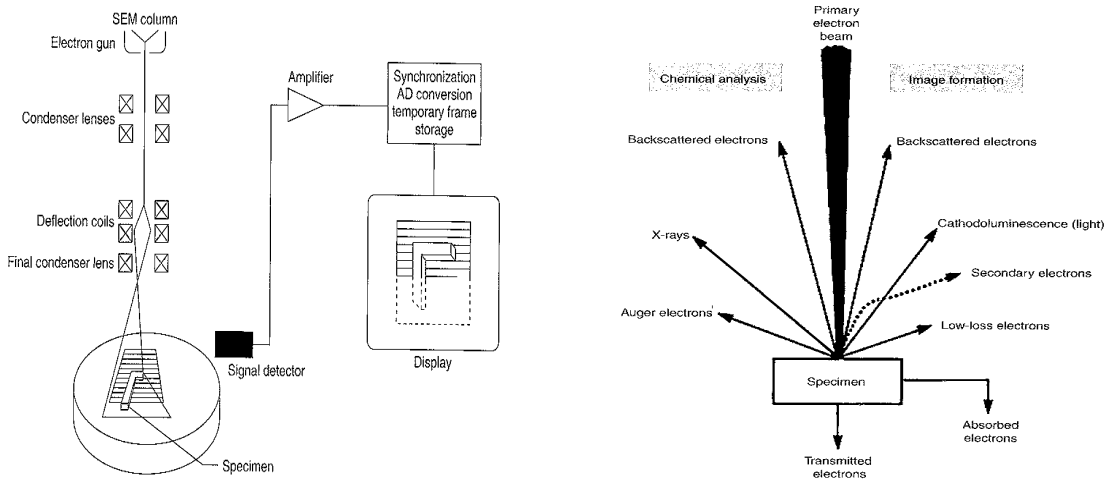

Figure 6: Left: a principle sketch of the SEM and the image formation. Right: an overview of the different signals that are generated when the electron beam hit the sample (the left Figure is obtained from [29], the right Figure is obtained from [30]).

Many signals are released from the sample when the electron beam hits[29]. Figure 6 (right) shows an overview of the different signals that appears when a sample is hit by the electron ray. The most common signals are secondary electrons (SE) and back-scattered electrons (BSE), but others like X-rays and Auger-electrons are also released[30]. The amount that is released and the amount detected by the sensors depends on the SEM used, the sample, and the voltage used to accelerate the electron beam.

The SE are released due to the collision between the incoming electrons and the sample surface[31]. Since the SE have a low energy, they only originate from the surface layer of

the sample (SE generated deeper does not have enough energy to escape from the sample) and consequently only contributes with information from the surface of the sample which mainly gives a topography-contrast[31].
The BSE are electrons from the original beam which are reemitted back from the sample[31]. The BSE contains much higher energy compared to the SE and can therefore give information from deeper levels of the sample[31]. They also give information about differences in the atomic number for different areas of the sample, where areas with higher atomic numbers appear brighter than areas with lower atomic number[31]. This is called material contrast or atomic number contrast.

2.2.3 Focused Ion Beam (FIB)

A focused ion beam (FIB) instrument resembles the SEM, but sends a ray of ions instead of a ray of electrons (which the SEM uses) onto the sample[32]. A schematic sketch of the source and the lenses in the FIB is shown in Figure 7. The ions are generated from a liquid metal ion source (LMIS) and sent out as a focused beam at the sample[32]. Since the ions would have been deflected and losing energy hitting other molecules, the operation needs to be performed in vacuum. Secondary ions or SE can then be detected by sensors to create an ion-induced SE-image[32]. Modern FIBs are so-called dual beam machines, which consist of a FIB and a SEM column. The SEM can be used to acquire high quality images from the FIB-created cross-sections.

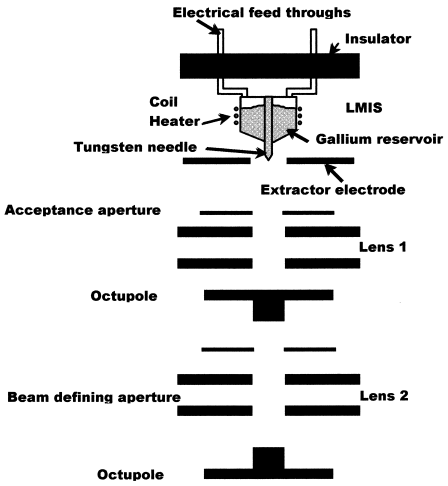

Figure 7: A principle sketch of the LMIS and the lenses in the FIB (the Figure is obtained from[32]).

One of the applications of the FIB is ion milling, where the ion ray is used to remove layers of the sample[32][33]. A pitch in the sample surface can be created (Figure 29), and then images can be taken of the cross-section in the same way as with the SEM.

Before the pitch is created, it is normal to deposit a layer of a material that is not easily removed by the ion beam (can be seen as a white bar over the pitch in Figure 29). This is done by injecting a suitable gas (containing the material being deposited) through a needle which is placed ∼100-200 μm from the sample surface (so-called gas assisted deposition)[32]. The ion beam is then rastered over the sample and interacts with the gas-molecules close to the surface which creates a local deposition[32]. The aim of having such a deposit is to create a sharp edge and an even sample cross-section (see the cross-section and deposition in Figure 29). This is a good method to investigate the interior of a sample, especially if the sample surface is contaminated, damaged, or difficult to be prepared with conventional methods such as mechanical polishing.

2.3 Electrochemical Principles and Techniques

2.3.1 Ohmic- and Polarization Resistance

The ohmic resistance (R_{ohmic}) is a measure of the resistance to charge transport in a conductor[34]. In fuel cells, R_{ohmic} is affecting both the electron transport between the two anodes and the ionic transport through the electrolyte, with the consequence of extra voltage loss (reduced cell voltage). The relation between the voltage loss and the resistance is given by Ohm's law:

$$\eta_{ohmic} = iR_{ohmic} = i(R_{elec} + R_{ionic}) \tag{6}$$

where η_{ohmic} is the ohmic voltage loss, i is the current, R_{elec} is the resistance from the electron transport, and R_{ionic} is the resistance from the ionic transport (normally R_{ionic} is much larger than R_{elec})[34].

With a constant cross-sectional area, R_{ohmic} is given by equation 7:

$$R_{ohmic} = \frac{l}{A\sigma} \tag{7}$$

where l is the transport length (travel distance) of the charge, A is the cross-sectional area of the conductor, and σ is the conductivity[34]. But in solid electrolyte conductors, the cross-sectional area tends to change and the transport length is normally not linear. These two phenomenas are described in section 2.1.1 as constrictivity (δ) and tortuosity (τ) respectively. The correlation between τ and δ with the ratio between the effective- and normal diffusion coefficient ($\frac{D_e}{D_b}$) is given by equation 4. But due to similarities between diffusion and conduction, equation 4 is also valid for electron- and ionic conduction[34][35]. It can therefore be rewritten as equation 8:

$$\frac{\sigma_e}{\sigma_b} = \frac{\Phi\delta}{\tau^2} \tag{8}$$

where σ_e is the effective conductivity, σ_b is the normal conductivity, and Φ is the volume fraction of the conductor. If equation 7 is inserted into equation 8, a relationship between ohmic resistance and microstructural properties is established:

$$\frac{R_b}{R_e} = \frac{\Phi\delta}{\tau^2} \tag{9}$$

where R_e is the effective ohmic resistance, and R_b is the normal ohmic resistance (note that $R_e \geq R_b$, where increased τ and a decreased δ and Φ increases the difference between the effective resistance and the normalized resistance in a dense bar of a pure conductor). As can be seen from equation 9, the ohmic resistance is dependent on tortuosity, constrictivity, and the volume fraction of the conductor.

The polarization resistance (R_p), or interfacial resistance (which it is also called), is the resistance towards electrochemical reactions on an electrode surface[36]. In other words, the higher the polarization resistance the lower the catalytic activity[36]. R_p can be derived from the famous Butler-Volmer equation:

$$j = j_0 \left(e^{\frac{\alpha n F \eta_{act}}{RT}} - e^{\frac{-(1-\alpha) n F \eta_{act}}{RT}} \right) \tag{10}$$

where j is the current density, j_0 is the exchange current density, α is the transfer coefficient, η_{act} is the activation voltage loss, R is the gas constant, T is the absolute temperature, n is the electron transfer coefficient, and F is the Faraday's constant[37]. For small values of η_{act}, normally less than 15 mV at room temperature (though at higher temperatures which are used in this work, this value can be larger) equation 10 can due to Taylor series ($e^x \simeq 1 + x$) be written as equation 11 [37].

$$\eta_{act} = \frac{jRT}{j_0 nF} \tag{11}$$

Equation 11 is of the same form as Ohm's law, and the resistance term in the equation which is given as:

$$R_p = \frac{RT}{j_0 nF} \tag{12}$$

is defined as the polarization resistance (in [38] R_p is written in another way). As can be seen from equation 12, the polarization resistance is inverse of the current exchange density. The speed (kinetics) of an electrochemical reaction is governed by j_0[37]. A high value of j_0 (and consequently a low value of R_p) is desirable for having a high reaction kinetics.

2.3.2 Area-Specific Resistance (ASR)

Area-specific resistance (ASR) is a resistance value which takes into account the size of the system being measured[39]. ASR is especially useful for R_{ohmic}, since it is so

dependent on the conductor area[39]. Since bigger fuel cells have more area where the current can flow through, the resistance is therefore lower compared to smaller fuel cells. To be able to compare the resistance between different fuel cells independently of their sizes, the ASR-value is used instead of the measured resistance. ASR is given by equation 13:

$$ASR = A_{fuelcell} \cdot R_{tot} \tag{13}$$

where $A_{fuelcell}$ is the cell area, and R_{tot} is the total resistance[39]. Since increased conductor length (or conductor thickness) also increases R_{tot}, ASR can also be used to compare different cells with different conductor lengths[39]. ASR for this case is then given by:

$$ASR = \frac{l}{\sigma} \tag{14}$$

where l is the conductor length, and σ is the conductivity[39].

2.3.3 Electrochemical Impedance Spectroscopy (EIS)

The electrochemical impedance spectroscopy (EIS) is an electrochemical characterization technique which can provide distinction between ohmic, activation, and concentration losses[40]. This in contrast to most other electrochemical characterization methods which are more simple and give less information. The EIS is a so-called in situ characterization technique which means it measures the performance of the cell while in operation[40]. The drawbacks with the EIS is that it is time consuming, hard to use under high-power conditions, and it is not always easy to interpret the results[40].

The impedance is defined as the ratio between the time-dependent voltage $V(t)$ and the time-dependent current $i(t)$[40]:

$$Z = \frac{V(t)}{i(t)} \tag{15}$$

where the time-dependent voltage is given by:

$$V(t) = V_0 \cos(\omega t) \tag{16}$$

and the time-dependent current is given by:

$$i(t) = i_0 \cos(\omega t - \phi) \tag{17}$$

where V_0 and i_0 are the amplitudes of the voltage and current respectively, ω is the radial frequency, and ϕ is the phase shift between the voltage and the current[40]. The input voltage (or the input current) comes from an a.c. sinusoidal wave applied on top of the d.c. potential. Therefore the output current (or the output voltage) comes out as

a sinusoidal wave, but normally with a phase shift (ϕ) which is illustrated in Figure 8 [40].

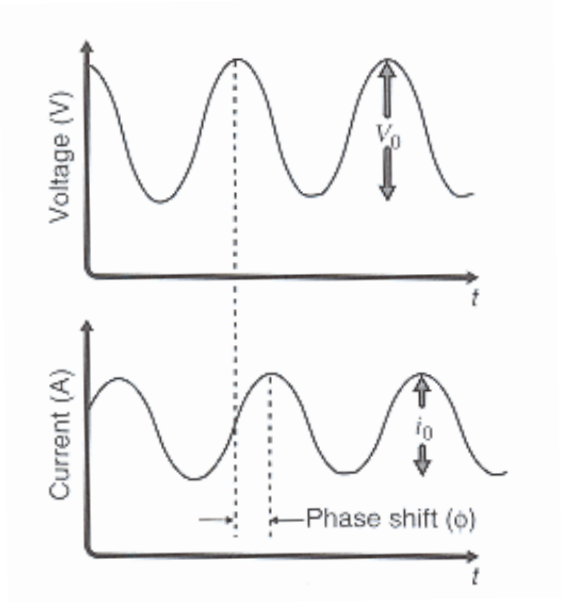

Figure 8: Time-dependent voltage (top) and time-dependent current (bottom) plotted against time. Normally there is a phase shift (ϕ) between them which is here illustrated(the Figure is obtained from [40]).

By inserting equation 16 and equation 17 into equation 15, Z is then given by:

$$Z = \frac{V_0 \cos(\omega t)}{i_0 \cos(\omega t - \phi)} = Z_0 \frac{\cos(\omega t)}{\cos(\omega t - \phi)} \tag{18}$$

where $Z_0 = \frac{V_0}{i_0}$[40]. Normally though, Z is instead given using a complex notation:

$$Z = \frac{V_0 e^{j_{im}\omega t}}{i_0 e^{(j_{im}\omega t - \phi)}} = Z_0 e^{j_{im}\phi} = Z_0(\cos\phi + j_{im}\sin\phi) \tag{19}$$

where j_{im} is the imaginary number ($j_{im} = \sqrt{-1}$) [40]. Equation 19 can be split into a real component ($Z_{re} = Z_0 \cos(\phi)$), and a imaginary part ($Z_{im} = j_{im} \cdot Z_0 \sin(\phi)$) which can be plotted in a so-called Nyquist plot shown in Figure 9 [40].

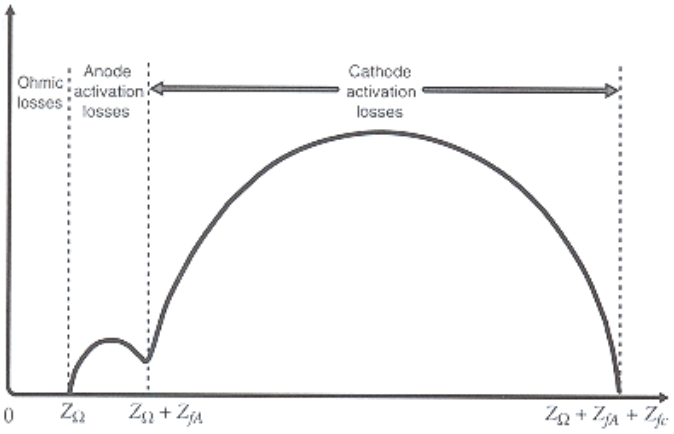

Figure 9: An illustration of a Nyquist plot where the real impedance (x-axis) is plotted against the negative imaginary impedance (y-axis). In this example the ohmic losses, the anodic activation losses, and the cathodic activation losses as well as their relative sizes can be seen (the Figure is obtained from [40]).

From the Nyquist plot, different losses can be observed (in this case the ohmic losses (Z_Ω), the anodic activation losses (Z_{fA}), and the cathodic activation losses (Z_{fc})) and their relative sizes. Very often the Nyquist plot can be hard to interpret and different losses can mask other losses[40]. Therefore is it important to obtain Nyquist plots at different d.c. current values by performing EIS-measurements at those values[40]. This increases the possibility for a better overview of the different losses that exist.

2.4 Microstructure Modeling of SOFC Anodes: Synthetic Microstructues for FEM

As mentioned earlier (section 2.1.1), suitable results for tortuosity (τ) and constrictivity (δ) can only be obtained from 3D-models, representing the anode microstructure. A 3D-model can be created from a stack of 2D-images obtained from FIB-tomography (section 2.2.3)[19]. FIB-tomography is very time consuming, and the microstructure needs to be represented by a large number of voxels in order to be representative. The large number of voxels may cause computing problems when using this 3D-model as structural input for finite element modeling (FEM). For efficient simulation of electrode reactions (by FEM), the morphological grid representing the microstructure must be simplified.

Another option for the morphological grid representation is then to create a computer made (artificial) 3D-model of the microstructure[19]. The model should be as accurate as possible compared to a real microstructure, despite the reduction of grid points compared to the models from FIB-tomography[41]. In this study synthetic microstructures are created by placing cubic particles of electronic (Ni) and mixed conducting phases (CGO) in a 3D-grid. Thereby the size of the particles and the corresponding volume

fractions were chosen according to the PSDs which were measured from real anode microstructures (in 2D). To ensure that the model is satisfactory, comparison between results obtained from the synthetic 3D-models with results from real microstructures are performed. The framework used for simulation of anode performance in this work is given in [17].

3 Experimental

3.1 Sample Preparation

3.1.1 Anode Fabrication and RedOx-Cycling

The Ni-CGO anodes were produced at Hexis (B. Iwanschitz) from powders from Praxair Speciality Ceramics[19]. Two different layers, the active anode layer and the current collector layer, were produced (see Figure 10). The active anode layers were composed of 50 wt% NiO and 50 wt% CGO, while the current collector layers were composed of 70 wt% NiO and 30 wt% CGO[19]. The powders were mixed with a terpineol based solution in a ball mill[19]. The two slurries were screen printed on a 3YSZ electrolyte as thin lamellas where the active anode layer was facing the electrolyte[19]. The anodes were sintered at 1350 ºC for 4 hours[19].

9 different samples were prepared, where the different samples were subjected from 0 to 8 redox-cycles. The samples were numbered from lamella 0 to lamella 8 according to the number of redox-cycles they were subjected to. The redox-cycles were performed at 950 ºC[9]. The reduction reactions were performed by the use of H_2-gas, and reoxidated by the use of O_2-gas from the post-combustion zone (more information can be obtained from [9]).

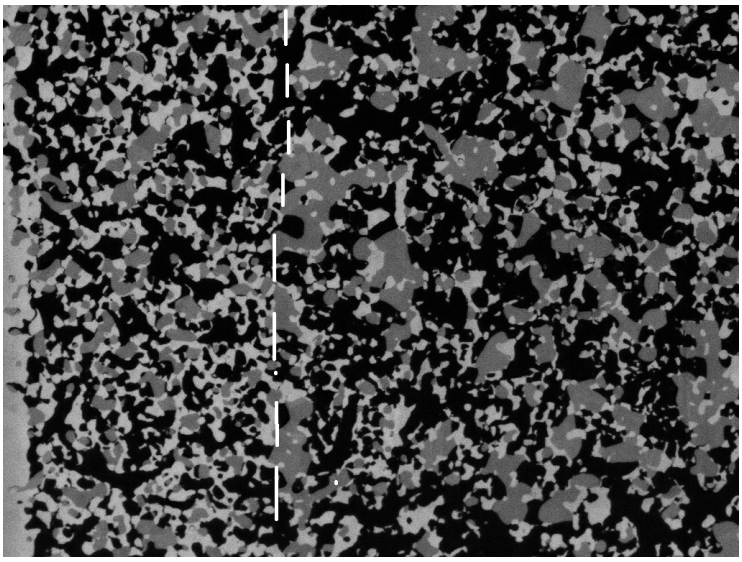

Figure 10: Illustration image of the active anode layer (left of the white stripes) and the current collector layer (right of the white stripes).

3.1.2 Sample Processing

Before the microscopic investigation, the lamellas had to be cut into small pieces and then they needed to be impregnated with an epoxy resin (Figure 11). A ratio of 4:1 of Araldite BY158 resin and Aradur hardener respectively were mixed and was then subjected to pressure ($\sim$ 2 bar for 12 hours). Then the samples in epoxy resin were ground and polished until their surface was even and transparent.

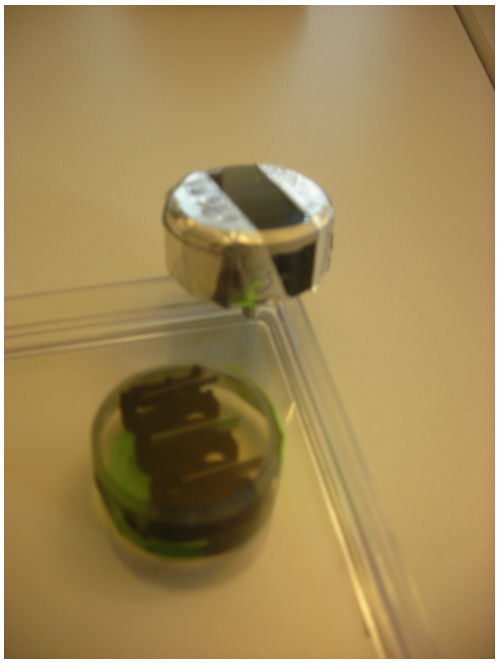

Figure 11: Bottom: thin sample-lamellas encapsulated in an epoxy resin, which has been grounded and polished. Top: sample-containing epoxy resin, which has been wrapped in aluminum foil to prevent charge accumulation in the SEM or in the FIB.

3.1.3 Carbon Coating Process

All the carbon thread coating of samples was performed using a MED020 Bal-Tec (Figure 12) located at EMPA Dübendorf (see section 2.2.1 or [28] for more information about the technical principles of the apparatus). The carbon threads were stretched between two high current electrodes (see Figure 5)[28]. The sample was placed beneath the carbon threads and a glass cylinder and a Plexiglas cover were placed around isolating the sample and the threads from the exterior, creating a chamber (Figure 5). The chamber was evacuated, up to a vacuum pressure of $5 \cdot 10^{-4}$ mbars. A low current was passed through the carbon threads, burning off impure carbon from the thread. Before this process, a movable shutter was positioned between the threads and the sample, protecting the sample from the heat and from the pollutants[28]. After approximately 10 seconds, the current was first reduced to zero and the shutter was turned away. A high current was then passed through the carbon threads, burning them off, which results in a thin carbon deposit on the sample surface. The chamber was then vented, and the coated sample could be collected.

Figure 12: The MED020 Bal-Tec apparatus which was used during the experiments. The glass cylinder and the Plexiglas enveloping the chamber can be seen to the left.

3.2 Sample Imaging

3.2.1 Scanning Electron Microscope (SEM)

All the SEM-analyses were performed using a Nova NanoSEM 230 from FEI at EMPA Dübendorf (see section 2.2.2 for more information about the technical principles of the SEM). The sample chamber was vented to atmospheric pressure and opened. A low voltage high contrast detector (vCD) was installed in the chamber for detection of BSE at $\leq$ 6 kV. A fix-installed Everhart-Thornley detector (ETD) was used to detect SE. A specimen holder was installed in the chamber and the sample was attached on top of it. The height of the specimen holder with the sample had to be adjusted so it would not damage the detectors. Before the sample was placed in the chamber, aluminum foil was wrapped around the sample (Figure 11) to ensure electron conductivity from the surface to the sample holder (preventing charge accumulation). The chamber was closed and evacuated to high vacuum. The sample was investigated by using the imaging parameters listed in Table 1. Quantitative analysis of the microstructures was performed on BSE-images.

3.2.2 Focused Ion Beam (FIB)

All the FIB-analyses of samples were performed using a NVision 40 Zeiss at ETH Zürich (see section 2.2.3 for more information about the technical principles of the FIB). The sample chamber was vented to atmospheric pressure and opened. A specimen holder was installed in the chamber and the sample was attached on top of it. The height of the specimen holder with the sample had to be adjusted so it would not damage the detectors. Before the sample was placed in the chamber, aluminum foil was wrapped around the sample (Figure 11) to ensure electron conductivity from the surface to the sample holder (preventing charge accumulation). The chamber was closed and evacuated to high vacuum. An energy and angle selective backscattered electron (ESB) detector was

used to detect the SE and create a visible picture. Carbon was deposited on the sample cross-section as a bar using a thin gas injection system (GIS)-needle (see section 2.2.3). This protective layer is necessary to create planar cross-sections and to prevent the formation of vertical stripes (called waterfall effect). The FIB was then used to create a cross-section of the anode perpendicular to the sample surface. The sample was studied with the use of the parameters listed in Table 1. An energy and angle selective backscattered electron (ESB) detector was used to create BSE-images.

Table 1: Overview of the parameters (high voltage (HV), working distance (WD), image width, spot size, aperture size, landing energy, resolution, bit depth, and pixel resolution) used during sample imaging by the SEM and the FIB.

Parameters	**SEM**	**FIB**
HV [kV]	5,0–6,0	1,70
WD [mm]	6,0	4,3
Image width [μm]	20	14.3/19.1
Spot size [-]	3,5	-
Aperture size [μm]	50	60
Landing energy [eV]	3,0–4,0	1,70
Matrix [pixels]	1024x943	1024x768
Bit depth [pixels]	8	8
Pixel resolution [nm]	19,4	14,0/18,7

3.3 Sample Analysis

3.3.1 Image Segmentation

All the image segmentations were performed using the software Matlab from Mathworks (see section 2.1.2 for an overview of image segmentation). An overview of the procedure is shown in Figure 13 [10].

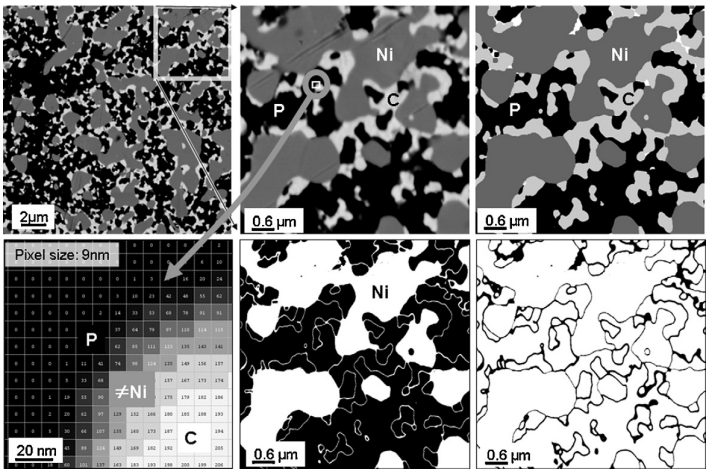

Figure 13: Procedure of the image segmentation. Top left: the original BSE-picture. Top centre: a magnified picture of the original-BSE picture. Top right: the finished segmented picture (though the white pixels are not yet distributed to a phase). Bottom left: An overview of the transition zone between the CGO-phase and the pore-phase. Bottom centre: Binary colour-picture after threshold segmentation between the phases (note that the transition zone is wrongly regarded as Ni). Bottom right: Binary picture showing the transition zones (in black) at phase boundaries, which make up to 15 % of the image (the Figure is obtained from [10]).

In the top left picture the original BSE-picture obtained from SEM is seen (Ni is the dark gray phase, CGO is the bright gray phase, and the pores are the black phase). An algorithm was used that first separates the different phases based on gray-scale (so-called thresholding). As can be seen, the transition zones (bottom left) between CGO and the pores are wrongly regarded as Ni (they both have the white colour). These transition zones were separated from the Ni-phase (bottom right), where they are black, while the phases are white. The transition zones were then distributed between the different phases which resulted in the final picture (top right). More information about this method can be found in [10].

3.3.2 Microstructural Parameter Extractions

As mentioned in section 2.1.1, the PSDs, TPBs, the volume fractions, the phase surface areas, and the phase interfacial areas of the different phases were measured in 2D. All the microstructural parameter extractions were performed using the software Java from Sun Microsystems/Oracle Corporation. The PSDs and volume fractions were obtained using the PSD_c-method (section 2.1.3). The TPB-pixels (the pixels which were in contact with all the three phases in the segmented picture) were counted from the BSE-pictures and normalized (divided) with the picture area. The surface areas were obtained by measuring the lengths of the circumference of the distinct phases and normalized with

the picture area. The interfacial areas were obtained by measuring the lengths of the contact lines between two different phases and normalized with the picture area.

The constrictivity and the tortuosity were measured from synthetic 3D models for the microstructure (section 2.4). Constrictivity was obtained by the use of the software Java from Sun Microsystems/Oracle Corporation, while tortuosity was obtained by the use of the software Avizo from the Visualization Sciences Group. The constrictivity was calculated by the difference between the PSD_c-method, which contains no constrictivity effect, and the MIP, which contains constrictivity effect because of the ink-bottle effect as described in section 2.1.3. The difference in the results between these two methods is regarded as the contribution from constrictivities. The experimental procedure for obtaining tortuosity is described in [42].

3.3.3 Electrochemical Impedance Spectroscopy (EIS)

All the impedance measurements were performed by Boris Iwanschitz at Hexis AG in Winterthur, Switzerland. The experimental procedure is described in the experimental part under the headline *Electrical and electrochemical characterization. - Impedance* in [9], but the EIS was in this case performed in a sealed button cell not an unsealed one which is written in [9].

4 Results

All the cross-section images analyzed were exclusively obtained by the FIB, while the images obtained from the SEM were not satisfactory (see Appendix A for more information). Results from lamellas 1, 4, 5, and 8 were chosen, while presenting results from all the lamellas was considered as unnecessary. To be able to maintain an acceptable aesthetic of the Figures was also a reason. For the active anode layer, lamella 7 is presented instead of lamella 8, since the quality of the cross-sections of the active anode layer from lamella 8 was not satisfactory.

4.1 Qualitative Comparison Between FIB Cross-Sectional Images

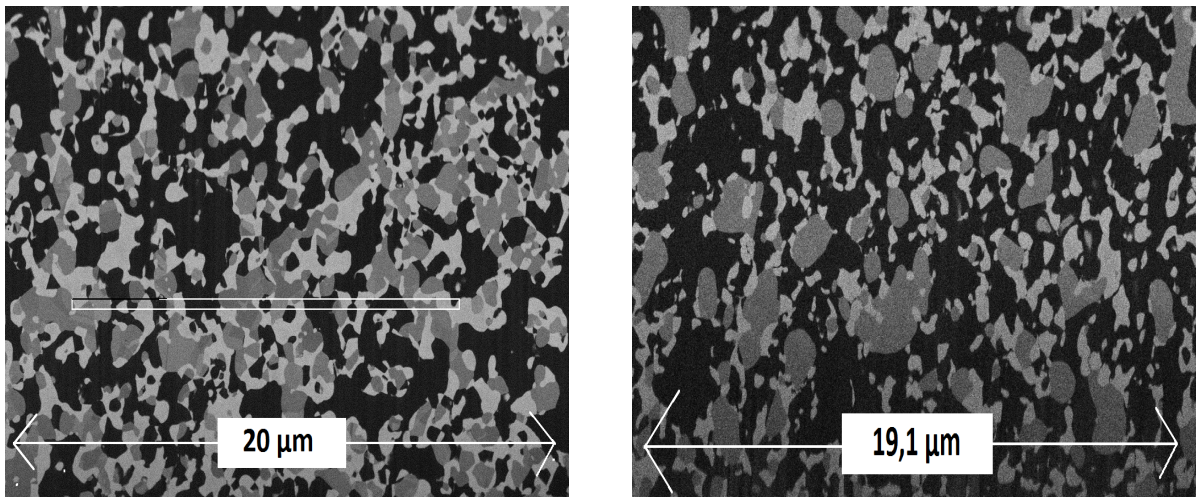

Figure 14: A FIB cross-sectional image from lamella 1 (left) and lamella 8 (right). The three different phases, pores (black), Ni (dark gray), and CGO (light gray) can be seen.

A cross-sectional image from lamella 1 (left) and from lamella 8 (right) obtained by the FIB are seen in Figure 14. The three phases, pores (black), Ni (dark gray), and CGO (light gray) can be seen. As can be seen in Figure 14, the Ni-grains in lamella 8 are larger and their number is smaller compared to lamella 1. The shape and the distribution of CGO are almost the same, while the amount of pores are higher in lamella 8 compared to lamella 1.

4.2 Continuous Phase Size Distributions (PSD_c)

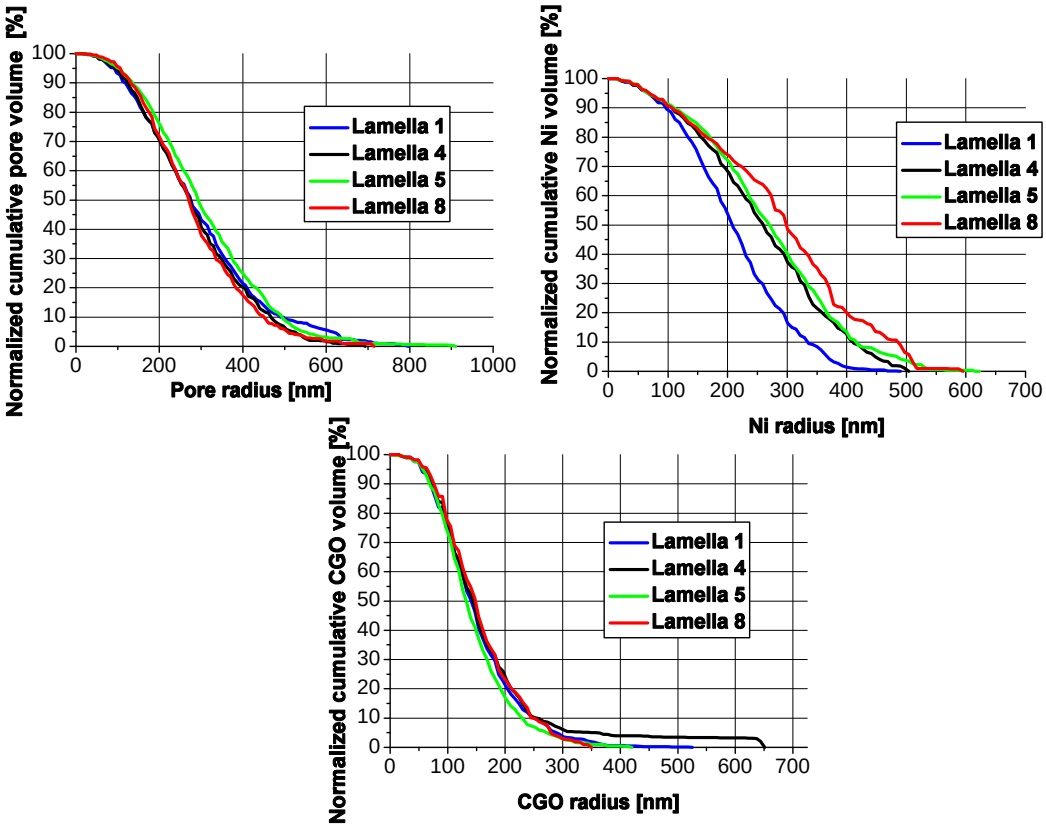

Figure 15: Normalized cumulative phase size distributions of pores (top left), Ni (top right), and CGO (bottom) from the current collector layer of lamellas 1, 4, 5, and 8.

Normalized cumulative phase size distributions for lamellas 1, 4, 5, and 8 from the current collector layer, are shown in Figure 15 for pores (top left), Ni (top right), and CGO (bottom). The curves are normalized to 100 %. The pore size distribution and the CGO size distribution remains stable from lamella 1 to lamella 8, while there is an increase of the Ni size distribution (Ni-coarsening) with increasing number of redox-cycles.

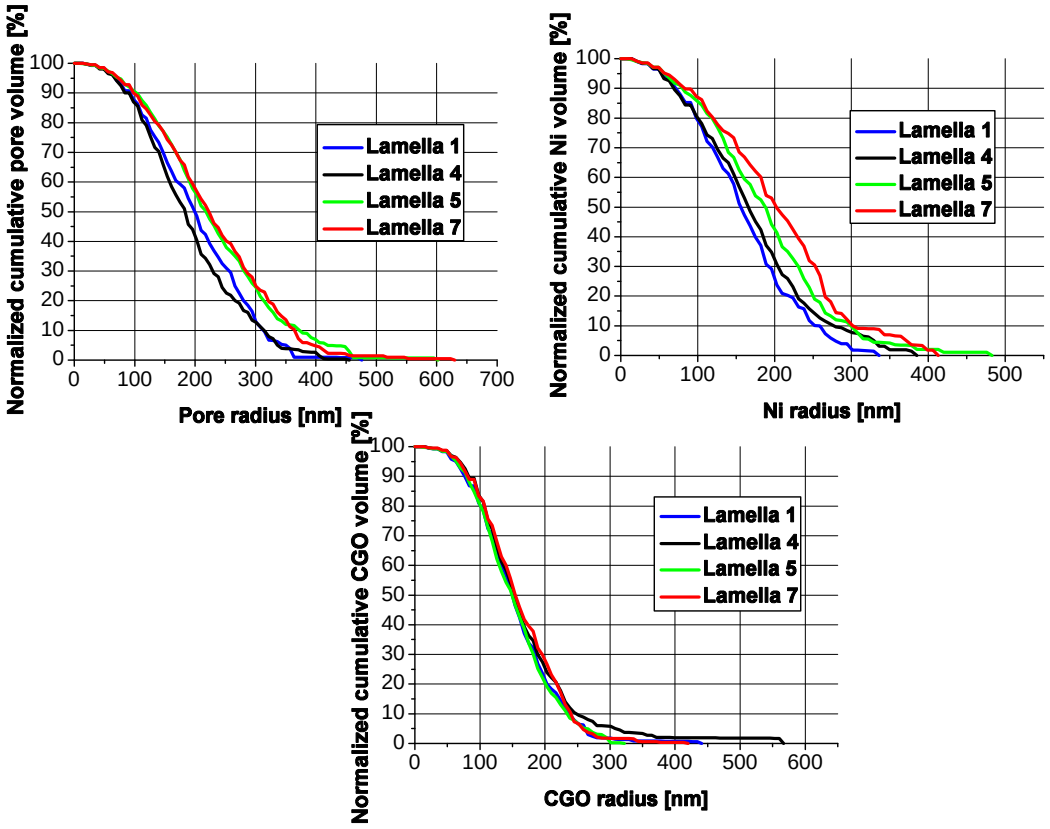

Figure 16: Normalized cumulative phase size distributions of pores (top left), Ni (top right), and CGO (bottom) from the active anode layer of lamellas 1, 4, 5, and 7.

Normalized cumulative phase size distributions for lamellas 1, 4, 5, and 7 from the active anode layer, are shown in Figure 16 for pores (top left), Ni (top right), and CGO (bottom). The curves are normalized to 100 %. The CGO size distribution remains stable from lamella 1 to lamella 7, while there is an increase of the Ni and pore size distributions (Ni- and pore-coarsening).

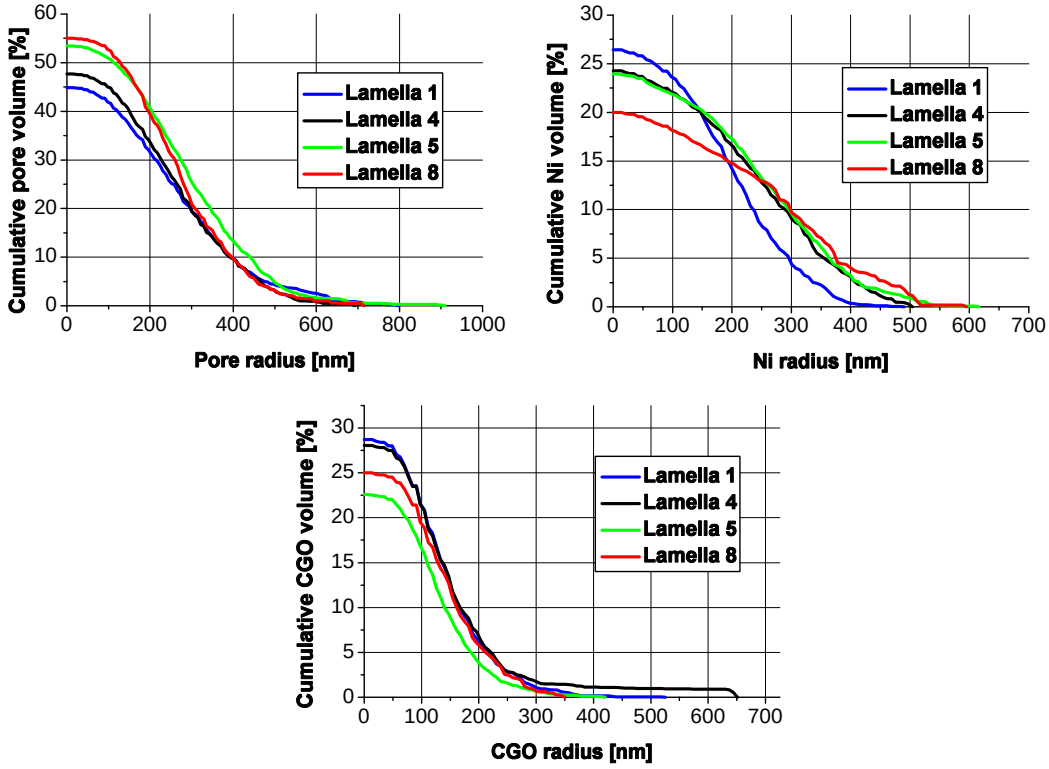

Figure 17: Cumulative phase size distributions of pores (top left), Ni (top right), and CGO (bottom) from the current collector layer of lamellas 1, 4, 5, and 8.

Non-normalized, cumulative phase size distributions for lamellas 1, 4, 5, and 8 from the current collector layer, are shown in Figure 17 for pores (top left), Ni (top right), and CGO (bottom). PSD-curves that are not normalized to 100 % contains information about changes of size and change of composition (phase volume fraction). An increase in small pores for lamellas 5 and 8 can be observed, while all lamellas have roughly the same amount of large pores. Lamellas 5 and 8 contains less Ni than lamellas 1 and 4, but larger Ni grains. Lamellas 1 and 4 contains more CGO than lamellas 5 and 8, but lamella 1 has rougly the same amount of large CGO grains as lamellas 5 and 8. The largest fraction of CGO grain sizes of lamella 4 is believed to be inhomogeneous regions of large CGO grains, and therefore wrongly shows large CGO grain sizes. In summary, there is an increase of (small) pores, which corresponds with a relative decrease of the solid phases.

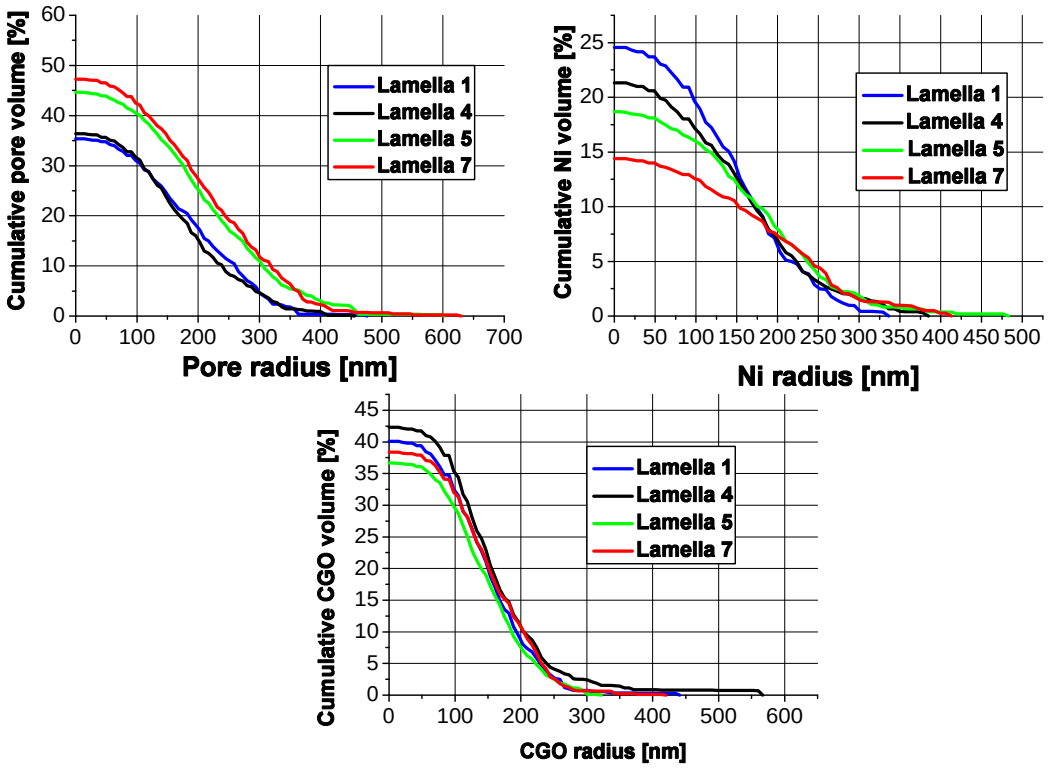

Figure 18: Cumulative phase size distributions of pores (top left), Ni (top right), and CGO (bottom) from the active anode layer of lamellas 1, 4, 5, and 7.

Non-normalized, cumulative phase size distributions for lamellas 1, 4, 5, and 7 from the active anode layer, are shown in Figure 18 for pores (top left), Ni (top right), and CGO (bottom). PSD-curves that are not normalized to 100 % contains information about changes of size and change of composition (phase volume fraction). Lamellas 5 and 7 have more pores than lamellas 1 and 4, and also more intermediate pores. All the lamellas have roughly the same amount of large pores. The largest fraction of pore sizes of lamella 7 is believed to represent an inhomogeneous region with exceptionally large pores. Lamellas 5 and 7 contain less Ni than lamellas 1 and 4, but larger Ni grains. Lamellas 1 and 4 contain more CGO than lamellas 5 and 7, but lamella 1 has rougly the same amount of large CGO grains as lamellas 5 and 7. The large CGO grain sizes of lamella 4 are believed to be an inhomogeneous region of large CGO grains, and therefore overestimates large CGO grain sizes.

4.3 Volume Fractions

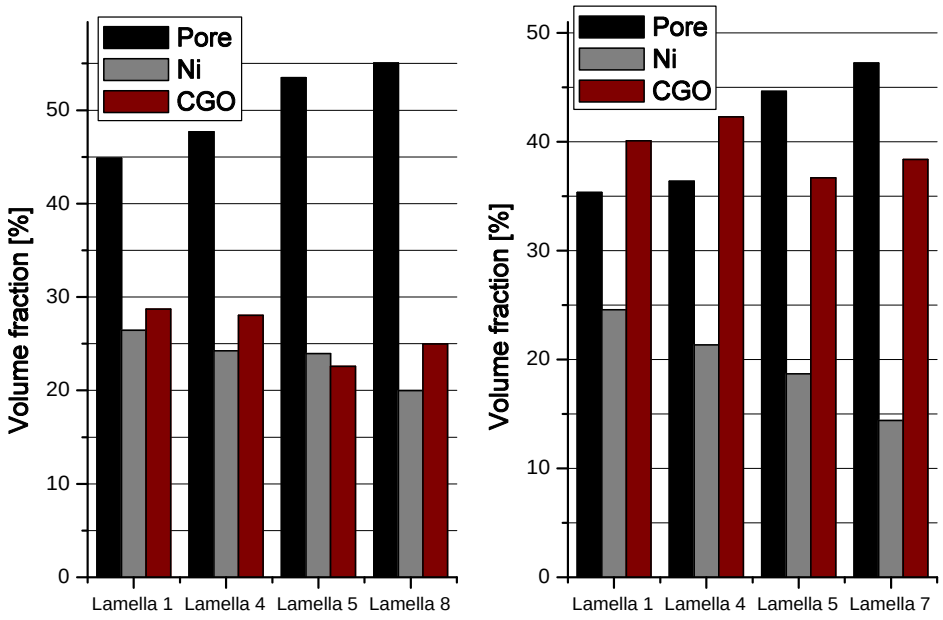

Figure 19: Volume fractions (Φ) for pores, Ni, and CGO from the current collector layer (left), and the active anode layer (right). Volume fractions are shown for lamellas 1, 4, 5, and 8 from the current collector layer, while volume fractions are shown for lamellas 1, 4, 5, and 7 from the active anode layer.

Volume fractions (Φ) for pores, Ni, and CGO from the current collector layer (left), and the active anode layer (right), are shown in Figure 19. For the current collector layer, the results from lamellas 1, 4, 5, and 8 are shown, while for the active anode layer, results from lamellas 1, 4, 5, and 7 are shown. In both layers the pore volume fraction increases with increasing lamella number (increasing number of redox-cycles), while the Ni volume fraction decreases. For the current collector layer, the CGO volume fraction generally decreases (though it increases between lamellas 5 and 8), while no distinct trend can be observed for the active anode layer.

4.4 Phase Surface Area

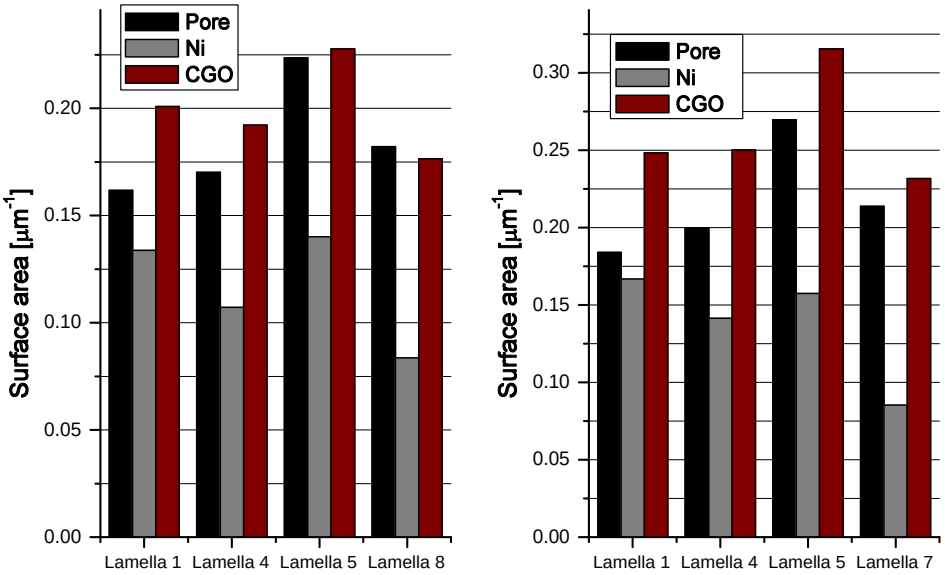

Figure 20: Phase surface areas for pores, Ni, and CGO from the current collector layer (left), and the active anode layer (right). The surface areas are shown for lamellas 1, 4, 5, and 8 from the current collector layer, while surface areas are shown for lamellas 1, 4, 5, and 7 from the active anode layer.

Phase surface areas for pores, Ni, and CGO from the current collector layer (left), and the active anode layer (right), are shown in 20. For the current collector layer, the results from lamellas 1, 4, 5, and 8 are shown, while for the active anode layer, results from lamella 1, 4, 5, and 7 are shown. For both layers there is a general increase of the pore surface area with increasing lamella numbers, while there is a general decrease for the Ni surface area. An exception from these patterns in both layers is lamella 5. For the CGO surface area, there is a general decrease in the current collector layer, with an exception in lamella 5. For the active anode layer, there is no distinct trend.

4.5 Phase Interfacial Area

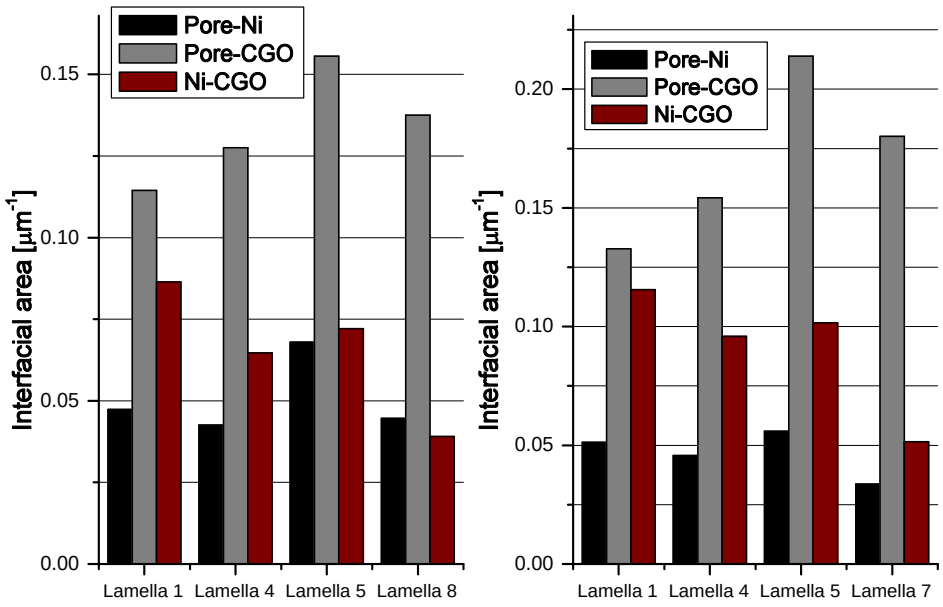

Figure 21: Interfacial areas between the pore-Ni, pore-CGO, and Ni-CGO phases from the current collector layer (left), and the active anode layer (right). Interfacial areas are shown for lamella 1, 4, 5, and 8 from the current collector layer, while interfacial areas are shown for lamella 1, 4, 5, and 7 from the active anode layer.

Interfacial areas between the pore-Ni, pore-CGO, and Ni-CGO phases from the current collector layer (left), and the active anode layer (right), are shown in Figure 21. For the current collector layer, the results from lamella 1, 4, 5, and 8 are shown, while for the active anode layer, results from lamella 1, 4, 5, and 7 are shown. For both layers the pore-CGO interfacial area increases from lamella 1 to 5, but then decreases. The pore-Ni interfacial area is generally constant for the current collector layer, with the exception of lamella 5. For the active anode layer it generally decreases, with the exception of lamella 5. For both layers the Ni-CGO interfacial area generally decreases, with an exception of lamella 5 for both layers.

4.6 Triple Phase Boundary (TPB) Changes

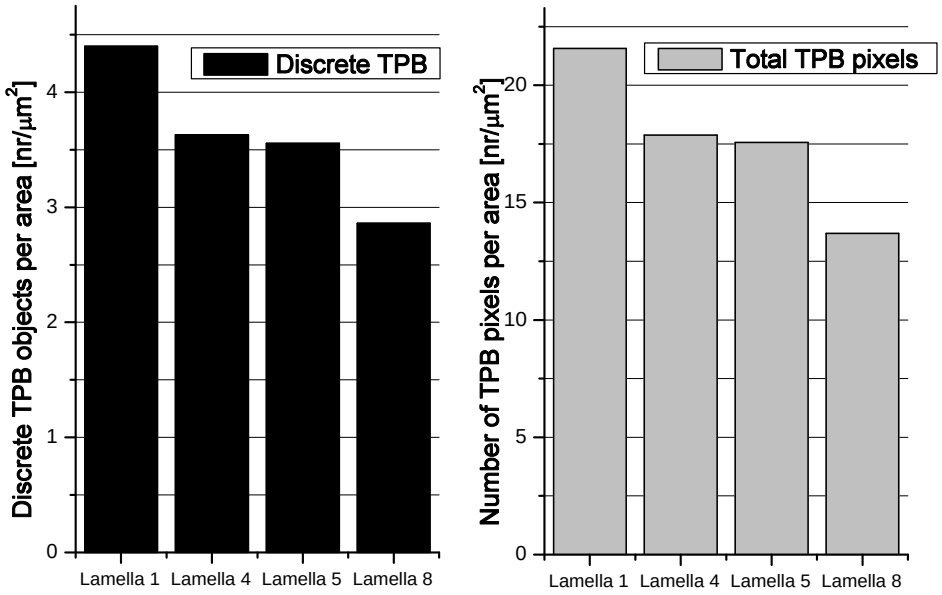

Figure 22: Normalized discrete TPB objects (left) and total number of TPB pixels (right) from the current collector layer for lamellas 1, 4, 5, and 8.

Discrete TPB objects and total number of TPB pixels from the current collector layer, both normalized with the picture area, are shown in Figure 22 for lamellas 1, 4, 5, and 8. Both the total number of TPB pixels and discrete TPB objects are decreasing from lamella 1 to 8.

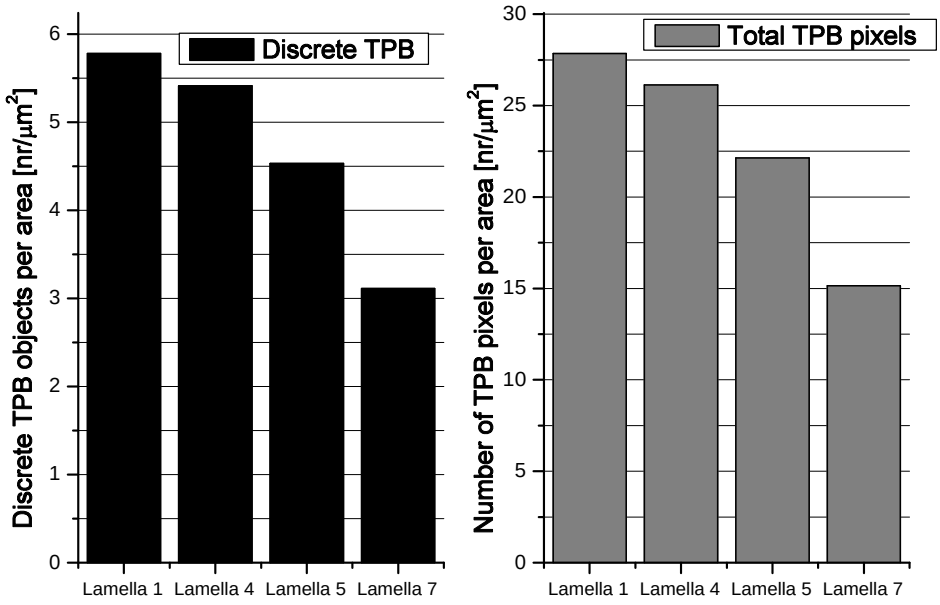

Figure 23: Normalized discrete TPB objects (left) and total number of TPB pixels (right) from the active anode layer for lamellas 1, 4, 5, and 7.

Discrete TPB objects and total number of TPB pixels from the active anode layer, both normalized with the picture area, are shown in Figure 23 for lamellas 1, 4, 5, and 7. Both the total number of TPB pixels and discrete TPB objects are decreasing from lamella 1 to 7.

4.7 Electrochemical Impedance Spectroscopy Results

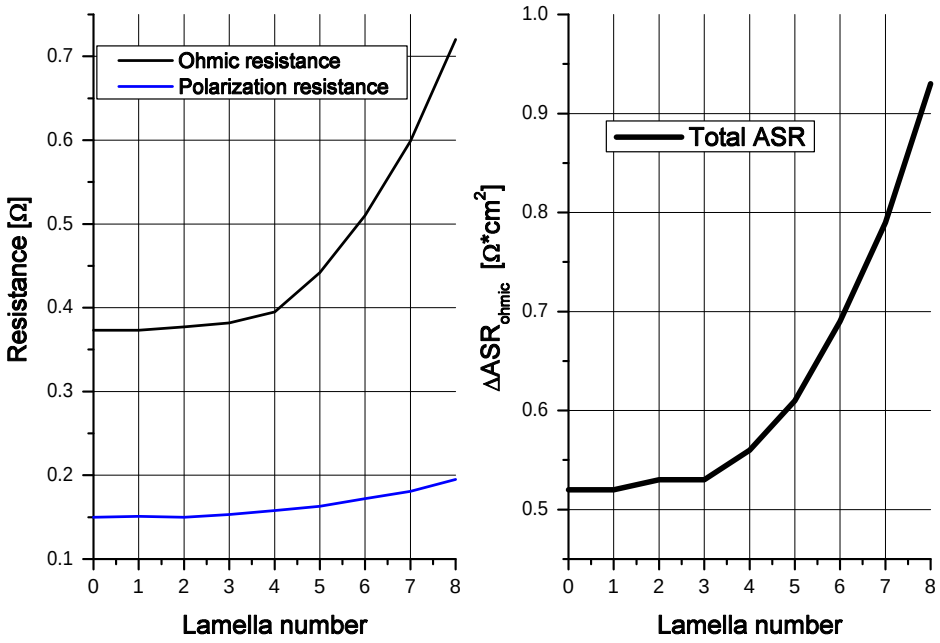

Figure 24: Ohmic- and polarization resistances (left), and the total area-specific resistance (ASR, right) from lamella 0 to 8.

The measured ohmic- and polarization resistances (R_{ohmic} and R_p respectively), and the total measured area-specific resistance (ASR) values for lamellas 0-8 are shown in Figure 24. The ohmic resistance is increasing rapidly from lamella 4 and outwards, while the polarization resistance just have a tiny increase. The total ASR-value increases rapidly from lamella 3, and shows a similar pattern as the ohmic resistance.

4.8 Analysis of Synthetic 3D-Microstructures

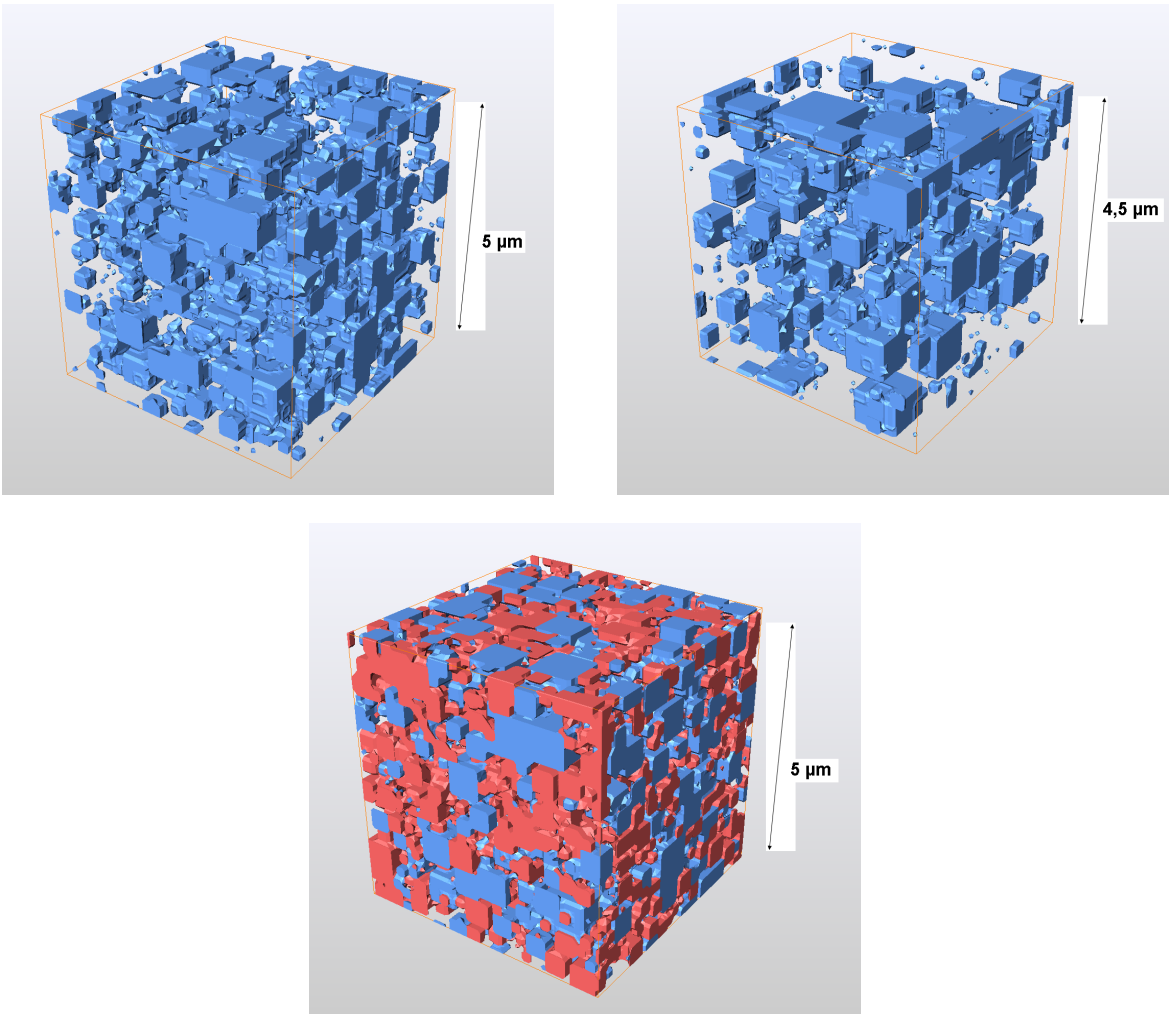

Figure 25: 3D-models representing the microstructure of the nickel phase (blue) in lamella 1 (left) and lamella 8 (right). The 3D-model at the bottom represents both solid phases (nickel = blue; CGO = red) in lamella 1. All the models consist of 50×50×50 voxels. The resolution for the models of lamella 1 (left and bottom) is 100 nm (edge length of the voxels), while the resolution for lamella 8 (right) is 89 nm voxel size. All synthetic models represent the microstructures of the current collector layers.

A 3D-model of the Ni phase from lamella 1 (left), lamella 8 (right), and a model of the Ni and the CGO phase from lamella 1 (bottom), can be seen in Figure 25. All the models are simulations of the current collector layer. A comparison between the Ni phase from lamella 1 (left), and the Ni phase from lamella 8, shows a clear coarsening of the Ni phase from lamella 1 to lamella 8. The Ni phase is mostly disconnected (no contact between the different Ni grains), especially for lamella 8. As can be seen from

the combined Ni+CGO-model (bottom), the combined Ni+CGO connectivity is much higher than the Ni connectivity.

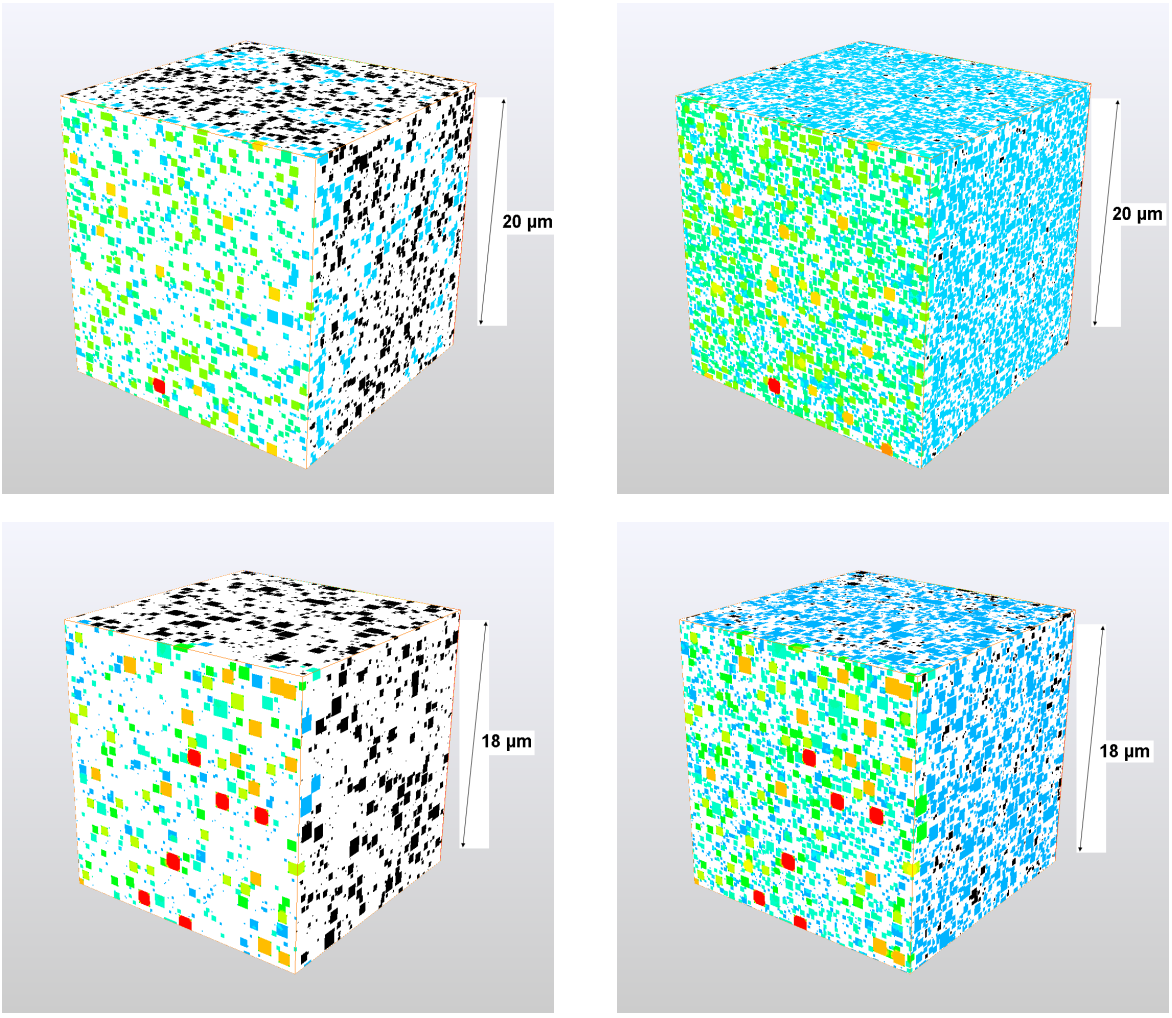

Figure 26: 3D-models representing the Ni phase (left side) and the total solid volume with Ni and CGO (right side). Thereby the upper models represent the microstructure after 1 redox-cycle, whereas the lower two models reflect microstructures after 8 redox-cycles. The colours indicate the size, which is obtained from MIP simulations, whereby red is maximum size and blue is minimum size after passing narrow pore necks. Black voxels represent Ni which is disconnected from the conducting network. All the models consist of 200×200×200 voxels. The resolution for lamella 1 (top left and bottom left) is 100 nm, while the resolution for lamella 8 (top right and bottom right) is 89 nm. All synthetic models represent the microstructures of the current collector layers.

The synthetic 3D-models from Figure 25 are taken as a basis for MIP-simulations in order to study the effect of constrictions on the pore size distributions and phase connectivity. The results of the MIP-simulations are shown in Figure 26 for lamella 1

(upper models) and for lamella 8 (bottom), whereby the colours indicate the constricted MIP-radii (red=maximum size of 350 nm, blue=minimum size of 100 nm, black=isolated grains, disconnected from the conducting network). The intrusion was started on the front-left plane towards back-right. For the models on the left side, the simulation was performed under the assumption that only the nickel phase is electrically conducting. As can be seen by the change in colour of the left models, the Ni network is not percolating, and the intrusion stops after a few voxels. In contrast, if the MIP-simulations are performed through the entire solid network (Ni+CGO models on the right side), this results in a high connectivity (hardly any black voxels).

Table 2: The calculated fractions of the solid phase volume, the disconnected solid phase, and the effective solid phase volume obtained from MIP-simulation. The fractions are for the Ni phase from lamella 1 and 8, and for the solid phase (Ni+CGO) from lamella 1 and 8. All the results are from the current collector layer and are obtained from Figure 30 in Appendix B.

	Solid phase volume fraction [%]	**Disconnected solid phase [%]**	**Eff. solid phase volume fraction [%]**
Ni Lam 1	26,44	54,80	11,95
Ni+CGO Lam 1	55,18	0,57	54,87
Ni Lam 8	20,11	100,0	0
Ni+CGO Lam 8	45,30	10,50	40,55

Table 2 shows the measured volume fractions of the conducting solid phase, the disconnected fraction of the conducting solid phase, and the effective conducting solid volume fraction obtained from MIP-simulation. The results are for the Ni phase from lamella 1 and 8, and for the solid phase (Ni+CGO) from lamella 1 and 8. All the results are from the current collector layer and are obtained from Figure 30 in Appendix B.

It is clear from the results that the disconnected solid phase for Ni is much higher compared to the combined Ni and CGO solid phase. The amount of disconnected solid phase is also increasing from lamella 1 to lamella 8. Consequently, the effective solid phase volume fractions for Ni is lower compared to Ni+CGO, and there is a decrease from lamella 1 to lamella 8 due to the Ni-coarsening and increase of porosity. For lamella 8, the anode is totally dependent on CGO to conduct electrons and prevent a total cell failure, since the Ni phase has 0 % connectivity. What can also be seen, is a decrease in the solid phase from lamella 1 to lamella 8, indicating a volume increase of the anode.

5 Discussion

The most prominent features of the microstructure degradation due to redox-cycling, are Ni coarsening and an increase of porosity. The observed changes of the microstructure are subsequently discussed in a qualitative way in the context of the degradation mechanisms, and of their effect on the anode reaction mechanism.

What can be seen from Figure 24, redox-cycling leads to a rapid increase of the ohmic resistance after the fourth redox-cycle, and to a rapid increase of the total area-specific resistance (ASR) after the third redox-cycle. In contrast, the polarization resistance is increasing very little. As pointed out in section 2.3.1, the polarization resistance is dependent mainly on the reaction kinetics, while the ohmic resistance is dependent on the charge transport (electron and ion conductivity). Figure 24 clearly indicates that the redox-cycles have a minor influence on the reaction kinetics, while the charge transport is clearly affected after 3-4 redox-cycles.

Increase of Ni grain size (Ni-coarsening) can clearly be observed in Figures 14–18, and 25. As mentioned in the Introduction, Ni-coarsening is one of the major problems with Ni-based anodes in SOFC, and is responsible for the decrease of the anode performance. During redox-cycling, Ni becomes oxidized to NiO, which results in a volume increase, and reduced back to Ni, which results in a volume contraction. When NiO is reduced back to Ni, it tends to precipitate on the large Ni grains, making them larger (Ni agglomeration). This reduces the connectivity, since the Ni that connected the large grains together, is the same Ni that has precipitated on the large Ni grains (Figure 25). Reduced connectivity increases the Ohmic resistance, since the number of transport routes for the electrons is reduced, and the reduction of the cross-sectional area of Ni between the large Ni grains. Due to the decrease of Ni connectivity, more electrons are forced to go through the CGO phase (Figure 26 and Table 2). This increases the ohmic resistance due to a lower electrical conductivity of CGO than Ni.

Figure 19 shows a volume increase of pores with increasing redox-cycles. From Figures 17, 18, 20, and 21, there is an indication that the increased volume of pores is caused by the formation of new small pores, and not due to an expansion of the existing pores. As mentioned in the Introduction, irreversible volume expansion of Ni-based anodes are a problem when the anode is subjected to redox-cycles, and can severely damage the anode structure and therefore its performance. Because of the volume expansion of the anode when Ni is oxidized to NiO, and due to the not fully reversible volume contraction of the anode when NiO is reduced back to Ni, there is a net increase of the anode volume. This increases the pore volume fraction, and subsequently reduces the Ni and CGO volume fractions (Figure 19 and Table 2). With reduced volume fraction of Ni and CGO, there is a possibility that they can decrease below the percolation threshold. This is believed to contribute to the increase of ohmic resistance (section 2.1.1) due to the reduction of connectivity.

What can be seen from Figures 22 and 23, is a decrease of the TPBs both in the active anode layer and the current collector layer. As mentioned in the Introduction, this is believed to be due to the Ni-coarsening. The anode performance is normally decreasing due to reduction in TPBs. Therefore, a stronger increase of the polarization resistance than observed in Figure 24 was expected, since a reduction in the TPBs normally affects the kinetic reactions in the anode. This can indicate that the TPBs are not so crucial to a Ni-CGO cermet anode, since CGO is a mixed conductor (can conduct both electrons and ions). Reactions can therefore in principle take place on the whole CGO free surface (the pore-CGO interfacial area). As can be seen from Figure 21, the pore-CGO interfacial area is generally increasing, and is therefore believed to compensate for the reduction of TPBs. The pore-Ni interfacial area, where dissociation of the fuel takes place, decreases only slightly, and prevents therefore a large increase in the polarization resistance. CGO can also create "bridges" between isolated Ni grains, preventing a further increase of the ohmic resistance or a total failure of the anode when there is no Ni connectivity (Figures 25 and 26 and Table 2).

Synthetic microstructures were produced with the aim to use them for simulation of anode reaction by means of finite element modelling. For this purpose, the synthetic microstructures should capture the relevant microstructural features which control the physical properties of the real samples. Since transport appears to be important for the redox-investigations, it was of particular interest to study the transport relevant parameters such as connectivity and constrictivity. This was performed by means of mercury intrusion simulation based on the synthetic 3D-microstructures. However, the results from MIP-simulation indicate that the resolution of synthetic microstructures is not enough to capture constrictivity and tortuosity effects realistically. The dimensions of most of the bottle necks are below 100 nm and hence the size classes must be in the range of 10 nm, which is similar as the resolution of FIB-tomography.

Most Figures in the results part show that lamella 5 deviates from the pattern compared to the other lamellas. Especially a higher content of Ni and pores is observed compared to the other lamellas. This is documented in Figures 17 and 18, where lamella 5 has a higher total content of Ni and pores than expected. It is believed that this exceptional anode composition in lamella 5 reflects a local heterogeneity in the microstructure. Unfortunately the FIB cross-sections cover a relatively small image window. Therefore, such heterogeneities may strongly affect the microstructure analysis.

As discussed in Appendix A, the results obtained by the use of the SEM were not satisfactory. This is a strong evidence that mechanical polishing leads to artifacts, whereby CGO grains are removed from the sample surface. The FIB was therefore used to obtain all the cross-sectional images in this work.

6 Conclusions

The aim of this work was to understand the influence of the microstructure features of the Ni-CGO anode for use in a SOFC on its electrochemical performance during degradation caused by redox-cycling. If this influence is fully understood, it will be a big step forward in improving the SOFC-technology, which can contribute to a successful commercialization.

One such influence is believed to be between the large increase of the ohmic resistance and the reduction in Ni-connectivity. The reduced Ni-connectivity is believed mainly to be due to Ni-coarsening and the net volume increase of the anode. The reduced connectivity forces the electrons to go through the CGO phase, which has a lower electrical conductivity than Ni.

Another influence can be between the low increase of the polarization resistance and an almost constant reaction surface area. It was expected that the observed reduction of the TPBs would make the polarization resistance increase more. The fact that this was not observed, may suggest that the TPBs are not so important for the Ni-CGO anode as expected. The fact that the CGO is a mixed conductor, and that the pore-CGO interfacial area increases with increasing number of redox-cycles, indicates that this surface compensates for the lost TPBs. The CGO probably also prevents a further increase of the ohmic resistance, since it offers an alternative path for the electrons when the Ni-connectivity is reduced. When the Ni-connectivity is reduced to zero, it can prevent a total cell failure.

Investigating the influence the tortuosity and the constrictivity have on the ohmic resistance would have been interesting, since the ohmic resistance apparently has a large influence on the anode performance. Unfortunately, obtaining satisfactory tortuosity and constrictivity values proved to be unsuccessful. For further works, improvements to the 3D-model should therefore be conducted, to ensure that the influence of the tortuosity and the constrictivity on the anode performance is fully understood. The role of the TPBs and the pore-CGO interfacial area in Ni-CGO anodes should also be investigated further.

7 References

[1] O'Hayre, R.; Cha, S.-W.; Colella, W.; Prinz, F.B.; *Fuel Cell Fundamentals*; John Wiley & Sons; New York; 2006; pp. 3–5.

[2] O'Hayre, R.; Cha, S.-W.; Colella, W.; Prinz, F.B.; *Fuel Cell Fundamentals*; John Wiley & Sons; New York; 2006; p. 6.

[3] Larminie, J.; Dicks, A.; *Fuel Cell Systems Explained*; 2. edition; John Wiley & Sons Ltd; Chichester; 2003; in *Foreword to the first edition*; Acres, G.

[4] O'Hayre, R.; Cha, S.-W.; Colella, W.; Prinz, F.B.; *Fuel Cell Fundamentals*; John Wiley & Sons; New York; 2006; p. 8.

[5] O'Hayre, R.; Cha, S.-W.; Colella, W.; Prinz, F.B.; *Fuel Cell Fundamentals*; John Wiley & Sons; New York; 2006; pp. 244–247.

[6] Larminie, J.; Dicks, A.; *Fuel Cell Systems Explained*; 2. edition; John Wiley & Sons Ltd; Chichester; 2003; pp. 207–212.

[7] Minh, N.Q.; *Ceramic Fuel Cells*; in *Journal of the American Ceramic Society*; volume 76 [3] (1993); p. 564.

[8] Cheng, Z.; Wang, J.-H.; Liu, M.; *Chapter 2. Anodes*; in *Solid Oxide Fuel Cells*; Fergus, J.W.; Hui, R.; Li, X.; Wilkinson, D.P.; Zhang, J.; CRC Press; Boca Raton; 2009; pp. 73–75.

[9] Iwanschitz, B.; Sfeir, J.; Mai, A.; Schütze, M.; *Degradation of SOFC Anodes upon Redox Cycling: A Comparison Between Ni/YSZ and Ni/CGO*; in *Journal of The Electrochemical Society*; volume 157 [2] (2010); pp. B269–B278.

[10] Holzer, L.; Iwanschitz, B.; Hocker, T.; Münch, B.; Prestat, M.; Wiedenmann, D.; Vogt, U.; Holtappels, P.; Sfeir, J.; Mai, A.; Graule, T.; *Microstructure degradation of cermet anodes for solid oxide fuel cells: Quantification of nickel grain growth in dry and in humid atmospheres*; in *Journal of Power Sources*; volume 196 (2011); pp. 1279–1294.

[11] Cheng, Z.; Wang, J.-H.; Liu, M.; *Chapter 2. Anodes*; in *Solid Oxide Fuel Cells*; Fergus, J.W.; Hui, R.; Li, X.; Wilkinson, D.P.; Zhang, J.; CRC Press; Boca Raton; 2009; pp. 101–121.

[12] Petersen, E.E.; *Diffusion in a Pore of Varying Cross Section*; in *The American Institute of Chemical Engineers*: volume 4 (1958); pp. 343–345.

[13] Clennell, M.B; *Tortuosity: a guide through the maze*; in *Developments in Petrophysics*; Lovel, M.A.; Harvey, P.K. in *Geological Society Special Publication* No. 122 (1997) pp. 299-344.

[14] van Brakel, J.; Heertjes, P.M.; *Analysis of Diffusion in Macroporous Media in Terms of a Porosity, a Tortuosity and a Constrictivity Factor*; in *International Journal of Heat and Mass Transfer*; volume 17 (1974); pp. 1093–1103.

[15] Cheng, Z.; Wang, J.-H.; Liu, M.; *Chapter 2. Anodes*; in *Solid Oxide Fuel Cells*; Fergus, J.W.; Hui, R.; Li, X.; Wilkinson, D.P.; Zhang, J.; CRC Press; Boca Raton; 2009; p. 78.

[16] Sunde, S.; *Monte Carlo Simulations of Conductivity of Composite Electrodes for Solid Oxide Fuel Cells*; in *Journal of the Electrochemical Society*; volume 143 [2] (1996); pp. 1123–1132.

[17] Costamagna, P.; Costa, P.; Antonucci, V.; *Micro-modelling of solid oxide fuel cell electrodes*; in *Electrochimica Acta*; volume 43 (1998); pp.375–394.

[18] O'Hayre, R.; Cha, S.-W.; Colella, W.; Prinz, F.B.; *Fuel Cell Fundamentals*; John Wiley & Sons; New York; 2006; pp. 76–78.

[19] Holzer, L; Münch, B.; Iwanschitz, B.; Cantoni, M.; Hocker, T.; Graule, T.; *Quantitative relationships between composition, particle size, triple phase boundary length and surface area in nickel-cermet anodes for Solid Oxide Fuel Cells*; in *Jounral of Power Sources*; volume 196 (2011); pp. 7076–7089.

[20] Pihlatie, M.; Kaiser, A.; Larsen, P.H.; Mogensen, M.; *Dimensional Behaviour of Ni-YSZ Anode Supports for SOFC Under RedOx Cycling Conditions*; in *The Electrochemical Society*; volume 7 (2007); pp. 1501–1510.

[21] Münch, B.; Holzer, L.; *Contradicting Geometrical Concepts in Pore Size Analysis Attained with Electron Microscopy and Mercury Intrusion*; in *Journal of the American Ceramic Society*; volume 91 [12] (2008); pp. 4059–4067.

[22] Golbert, J.; Adjiman, C.S.; Brandon, N.; *Microstructural Modeling of Solid Oxide Fuel Cell Anodes*; in *The American Chemical Society*; volume 47 (2008); pp. 7693–7699.

[23] Wilson, J.R; Kobsiriphat, W.; Mendoza, R.; Chen, H.-Y.; Hiller, J.M.; Miller, D.J.; Thornton, K.; Voorhees, P.W.; Adler, S.B.; Barnett, S.A.; *Three-dimensional reconstruction of a solid-oxide fuel-cell anode*; in *Nature Publishing Group*; volume 5 (2006); pp. 541–544.

[24] Cheng, Z.; Wang, J.-H.; Liu, M.; *Chapter 2. Anodes*; in *Solid Oxide Fuel Cells*; Fergus, J.W.; Hui, R.; Li, X.; Wilkinson, D.P.; Zhang, J.; CRC Press; Boca Raton; 2009; pp. 78–84.

[25] O'Hayre, R.; Cha, S.-W.; Colella, W.; Prinz, F.B.; *Fuel Cell Fundamentals*; John Wiley & Sons; New York; 2006; p. 144.

[26] Thilagamani, S.; Shanthi, N.; *A Survey on Image Segmentation Through Clustering*; in *International Journal of Research and Reviews in Information Sciences*; volume 1 (2011); p. 15.

[27] Russ, J.C.; *The Image Processing Handbook*; CRC Press LLC; Boca Raton; 1999; pp. 371–374.

[28] Publisher: Bal-Tec AG; Title: MED 020 Modular High Vacuum Coating System; (1999); Retrieved: 3 May, 2011; Web site: *nanosci.co.kr/app.htm → Coating → MED 020 Modular High Vacuum Coating System → Coating → MED 020 Modular High Vacuum Coating System*; pp. 3–4.

[29] Vladár, A.E.; Postek, M.T.; *The Scanning Electron Microscope*; in *Handbook of Charged Particle Optics*; 2. edition; CRC Press; Boca Raton; 2008; pp. 438–439.

[30] Vladár, A.E.; Postek, M.T.; *The Scanning Electron Microscope*; in *Handbook of Charged Particle Optics*; 2. edition; CRC Press; Boca Raton; 2008; pp. 452–453.

[31] Vladár, A.E.; Postek, M.T.; *The Scanning Electron Microscope*; in *Handbook of Charged Particle Optics*; 2. edition; CRC Press; Boca Raton; 2008; pp. 456–461.

[32] Giannuzzi, L.A.; Stevie, F.A.; *A review of focused ion beam milling techniques for TEM specimen preparation*; in *The International Research and Review Journal for Microscopy*; volume 30 (1999); pp. 197–204.

[33] Melngailis, J.; *Focused ion beam technology and applications*; in *Journal of Vacuum Science and Technology B*; volume 5 (1987); p. 483.

[34] O'Hayre, R.; Cha, S.-W.; Colella, W.; Prinz, F.B.; *Fuel Cell Fundamentals*; John Wiley & Sons; New York; 2006; pp. 93–99.

[35] Fan, Z.; *A microstructural approach to the effective transport properties of multiphase composites*; in *Philosophical Magazine A*; volume 73 (1995); pp. 1663–1684.

[36] Cheng, Z.; Wang, J.-H.; Liu, M.; *Chapter 2. Anodes*; in *Solid Oxide Fuel Cells*; Fergus, J.W.; Hui, R.; Li, X.; Wilkinson, D.P.; Zhang, J.; CRC Press; Boca Raton; 2009; pp. 90–92.

[37] O'Hayre, R.; Cha, S.-W.; Colella, W.; Prinz, F.B.; *Fuel Cell Fundamentals*; John Wiley & Sons; New York; 2006; pp. 66–86.

[38] Koide, H.; Someya, Y.; Yoshida, T.; Maruyama, T.; *Properties of Ni/YSZ cermet as anode for SOFC*; in *Solid State Ionics*; volume 132 (2000); pp. 253–260.

[39] O'Hayre, R.; Cha, S.-W.; Colella, W.; Prinz, F.B.; *Fuel Cell Fundamentals*; John Wiley & Sons; New York; 2006; pp. 100–103.

[40] O'Hayre, R.; Cha, S.-W.; Colella, W.; Prinz, F.B.; *Fuel Cell Fundamentals*; John Wiley & Sons; New York; 2006; pp. 201–224.

[41] Sunde, S.; *Simulations of Composite Electrodes in Fuel Cells*; in *Journal of Electroceramics*; volume 5 [2] (2000); pp. 153–182.

[42] Keller, L.M.; Holzer, L.; Wepf, R.; Gasser, P.; *3D geometry and topology of pore pathways in Opalinus clay: Implications for mass transport*; in *Aplied Clay Science*; volume 52 (2011); pp. 85–95.

Appendices

A Comparison of SEM- and FIB-Results

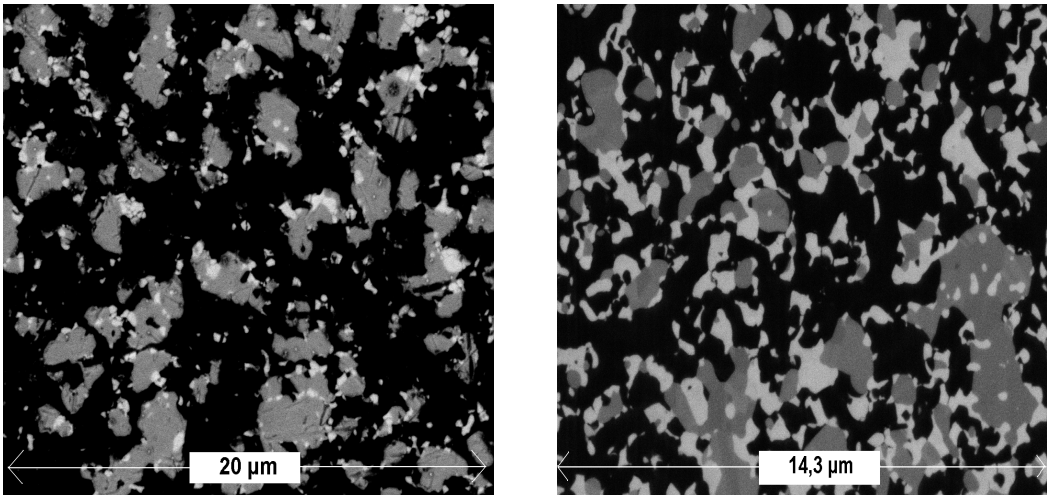

Figure 27: Microstucture of Lamella 5: polished surface and analyzed with the SEM (left) and FIB cross-section (right).

As stated in section 3.1.2, the lamellas were impregnated with an epoxy resin and were ground and polished until their surface was even and transparent. The SEM was chosen to obtain images of the microstructure for analysis. The reason for this was that the SEM is relatively fast to operate. But, as can be observed in Figure 27 (left) and Figure 28, the amount of pores (black phase on Figure 27) is very high and the amount of CGO (white gray phase on Figure 27) very low, which does not represent the true anode microstructure.

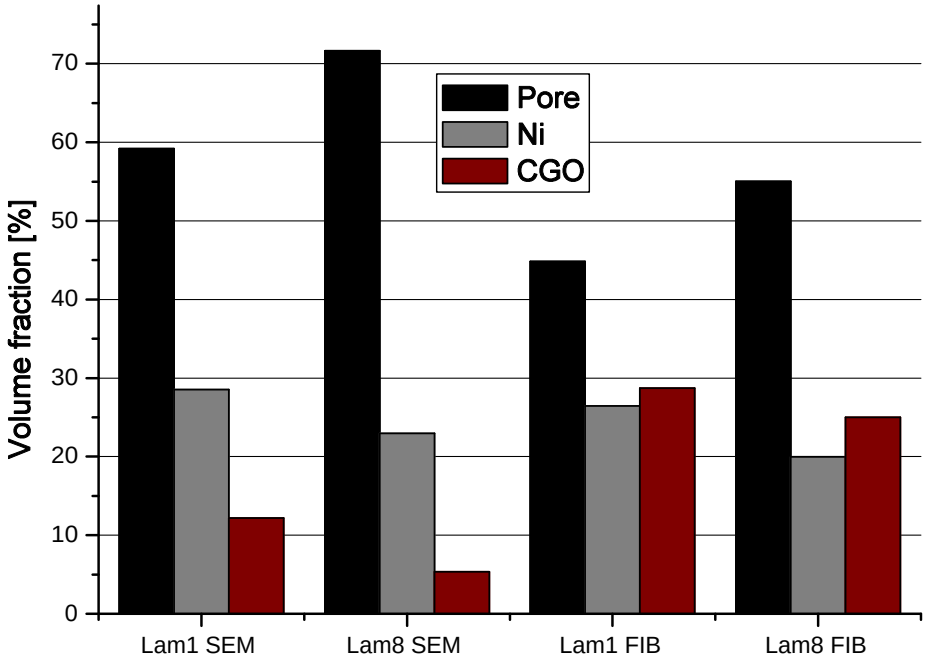

Figure 28: Volume fractions (Φ) of the pores, Ni, and CGO in lamellas 1 and 8 obtained from the SEM, and from lamellas 1 and 8 obtained from the FIB.

Cross-sections perpendicular to the polished surface of the samples were investigated by milling with the FIB (Figure 29). As can be seen from the cross-section from Figure 27 (right) and Figure 29, the amount of pores is lower, and the amount of CGO is higher compared to the analyses with the SEM. The FIB-cross-sections thus give a much better representation of the true anode microstructure.

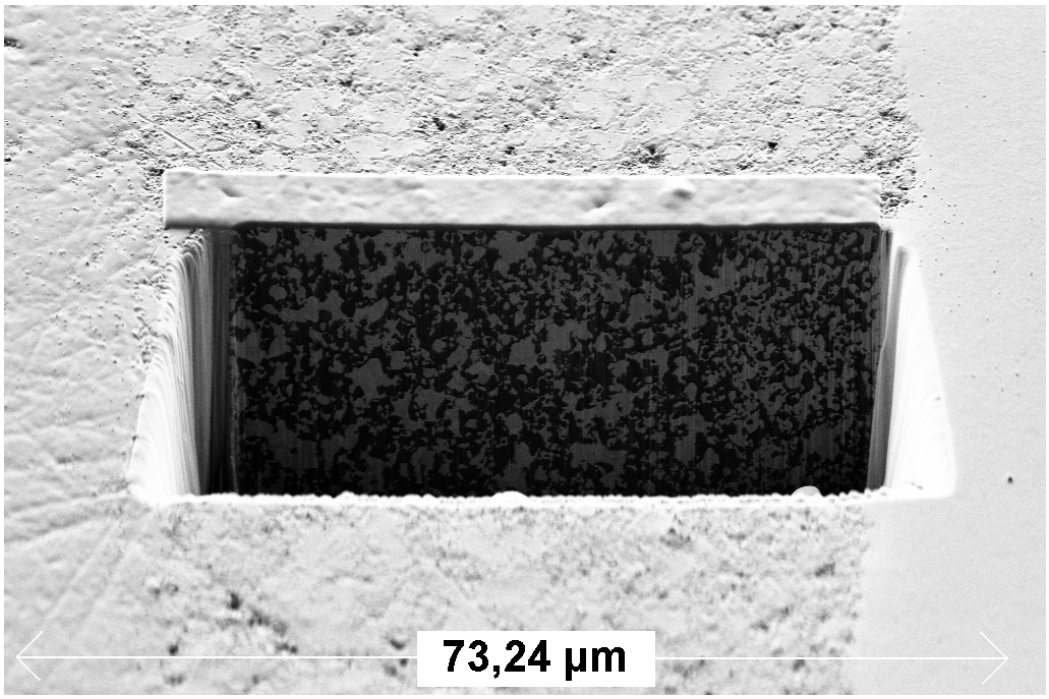

Figure 29: Cross-section picture of Lamella 7 from FIB.

By investigating Figure 29, which shows both the sample surface and the FIB cross-section, black holes and scratches on the sample surface can be observed. These damages are believed to originate from when the samples were ground and polished. CGO-grains are believed to be ripped off the sample surface, reducing the measured CGO-content. Consequently, the porosity is increased. The FIB cross-section is not affected from these damages, and by analyzing it instead of the sample surface is believed to give more accurate results. Consequently, the FIB was then exclusively used as a basis for quantitative microstructural analysis.

B Connectivity Calculations

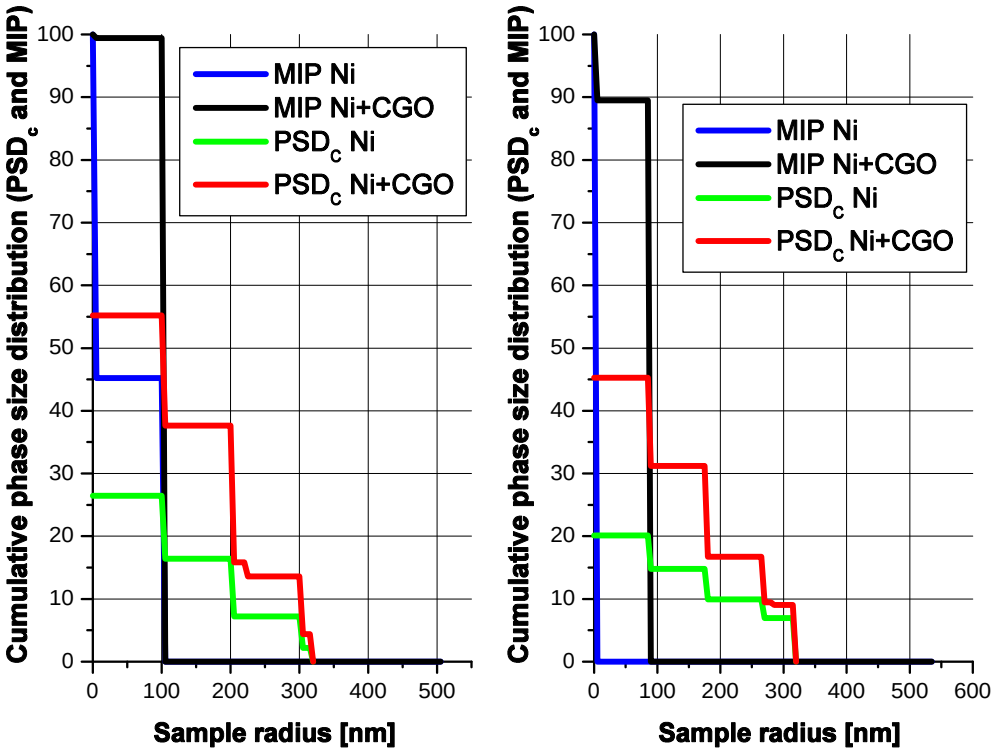

Figure 30: Cumulative phase size distributions and mercury intrusion porosimetry distributions for lamella 1 (left) and 8 (right) for Ni and Ni+CGO.

Non-normalized, cumulative phase size distributions and mercury intrusion porosimetry distributions for lamella 1 (left) and 8 (right) for Ni and Ni+CGO are shown in Figure 30. The values given in Table 2 are obtained from this Figure. The zero connectivity for Ni in lamella 8 can clearly be seen from the MIP curve. A much higher connectivity for Ni+CGO can be seen in both lamellas.